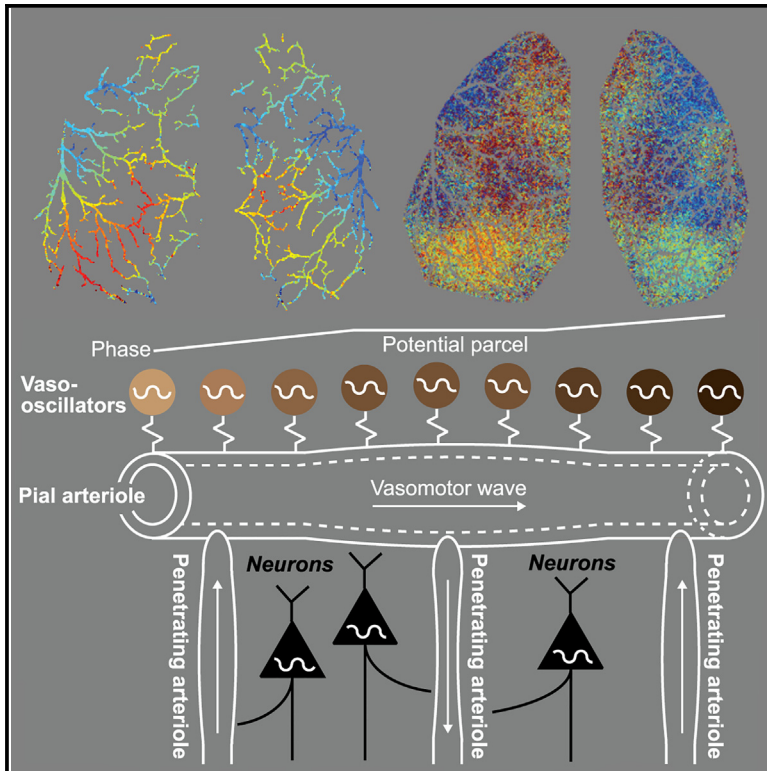# Neuron

Long-wavelength traveling waves of vasomotion modulate the perfusion of cortex

Graphical abstract

Authors

Thomas Broggini, Jacob Duckworth, Xiang Ji, ..., Massimo Vergassola, Gal Mishne, David Kleinfeld

Correspondence

dk@physics.ucsd.edu

In brief

Broggini, Duckworth, et al. assessed the physiological impact and spatiotemporal dynamics of the ~0.1 Hz oscillations in the diameter of neocortical arterioles in the awake mouse. They found that the oscillations within penetrating arterioles, which source blood from pial arterioles to the capillary bed, profoundly modulate resting-state perfusion throughout neocortex.

Highlights

- Vaso-oscillations in arteriole diameter modulate the perfusion of blood to cortex

- Modulation during the resting state exceeds that of stimulus-induced activity

- Vaso-oscillations support long-wavelength traveling waves along all arterioles

- Waves along penetrating arterioles are unlikely to translocate interstitial solutes

CellPress

Neuron

CellPress

Article

Long-wavelength traveling waves of vasomotion modulate the perfusion of cortex

Thomas Broggini,[1,2,3,10] Jacob Duckworth,[1,10] Xiang Ji,[1,11] Rui Liu,[1,11] Xinyue Xia,[4,11] Philipp Mächler,[1] Iftach Shaked,[1] Leon Paul Munting,[5] Satish Iyengar,[6] Michael Kotlikoff,[7] Susanne J. van Veluw,[5] Massimo Vergassola,[8] Gal Mishne,[4] and David Kleinfeld[1,9,12,*]

[1]Department of Physics, University of California, San Diego, La Jolla, CA 92093, USA
[2]Goethe University Frankfurt, Department of Neurosurgery, 60528 Frankfurt am Main, Germany
[3]Frankfurt Cancer Institute, Goethe University Frankfurt, 60528 Frankfurt am Main, Germany
[4]Halıcıoğlu Data Science Institute, University of California, San Diego, La Jolla, CA 92093, USA
[5]Department of Neurology, Massachusetts General Hospital, Boston, MA 02114, USA
[6]Department of Statistics, University of Pittsburgh, Pittsburgh, PA 15260, USA
[7]College of Veterinary Medicine, Cornell University, Ithaca, NY 14853, USA
[8]Laboratoire de Physique, Ecole Normale Supérieure, 75230 Paris, France
[9]Department of Neurobiology, University of California, San Diego, La Jolla, CA 92093, USA
[10]These authors contributed equally
[11]These authors contributed equally
[12]Lead contact
*Correspondence: dk@physics.ucsd.edu
https://doi.org/10.1016/j.neuron.2024.04.034

SUMMARY

Brain arterioles are active, multicellular complexes whose diameters oscillate at $\sim$ 0.1 Hz. We assess the physiological impact and spatiotemporal dynamics of vaso-oscillations in the awake mouse. First, vaso-oscillations in penetrating arterioles, which source blood from pial arterioles to the capillary bed, profoundly impact perfusion throughout neocortex. The modulation in flux during resting-state activity exceeds that of stimulus-induced activity. Second, the change in perfusion through arterioles relative to the change in their diameter is weak. This implies that the capillary bed dominates the hydrodynamic resistance of brain vasculature. Lastly, the phase of vaso-oscillations evolves slowly along arterioles, with a wavelength that exceeds the span of the cortical mantle and sufficient variability to establish functional cortical areas as parcels of uniform phase. The phase-gradient supports traveling waves in either direction along both pial and penetrating arterioles. This implies that waves along penetrating arterioles can mix, but not directionally transport, interstitial fluids.

INTRODUCTION

The arterioles that source blood to the brain are dynamic. The diameter of their elastic walls oscillates, driven by oscillation of smooth muscle cells that surround the arteriole wall. This process is referred to as vasomotion.[1,2] It occurs in a broad frequency band centered near 0.1 Hz in species as varied as rodent and human. Critically, vasomotor oscillations are observed in individual brain arterioles that are isolated and brought to physiological pressure and temperature.[3] Thus, brain arterioles must be considered as active organs, consistent with their role in autoregulation of arteriole flow,[4] as opposed to passive mechanical filters of the pressure waves and fluctuations in the underlying flow.

There are two functional classes of cortical arterioles.[5] The pial arterioles form a highly interconnected, two-dimensional network across the cortical mantle that distributes blood from the large cerebral arteries to the penetrating arterioles (PAs). The

PAs branch from the pial vessels and dive into the mantle to source the capillary bed, a three-dimensional network that delivers nutrients to brain cells. Past work established that changes in diameter of the pial arterioles can direct blood to areas of heightened neuronal activity.[6] Further, interruption to flow in any one branch of the pial network is compensated by a redirection of flow in neighboring vessels.[7] Of particular interest, pial vessels exhibit vasomotor oscillations.[8,9] Consistent with an intrinsic mechanism, these oscillations are maintained when cortical synaptic activity is blocked.[3,9] With regard to network dynamics, vasomotor oscillations can be partially entrained by neuronal activity.[8,10,11] Specifically, the $\sim$0.1 Hz component of the underlying neuronal signal has a peak correlation coefficient, or magnitude of spectral coherence, of $\sim$0.6 at the vasomotor frequency.[8]

The spatial aspect of vasomotion in brain arterioles is largely unexplored, and in PAs, the occurrence of even vasomotion, per se, is an open issue. Periodic wave motion, in the form of a
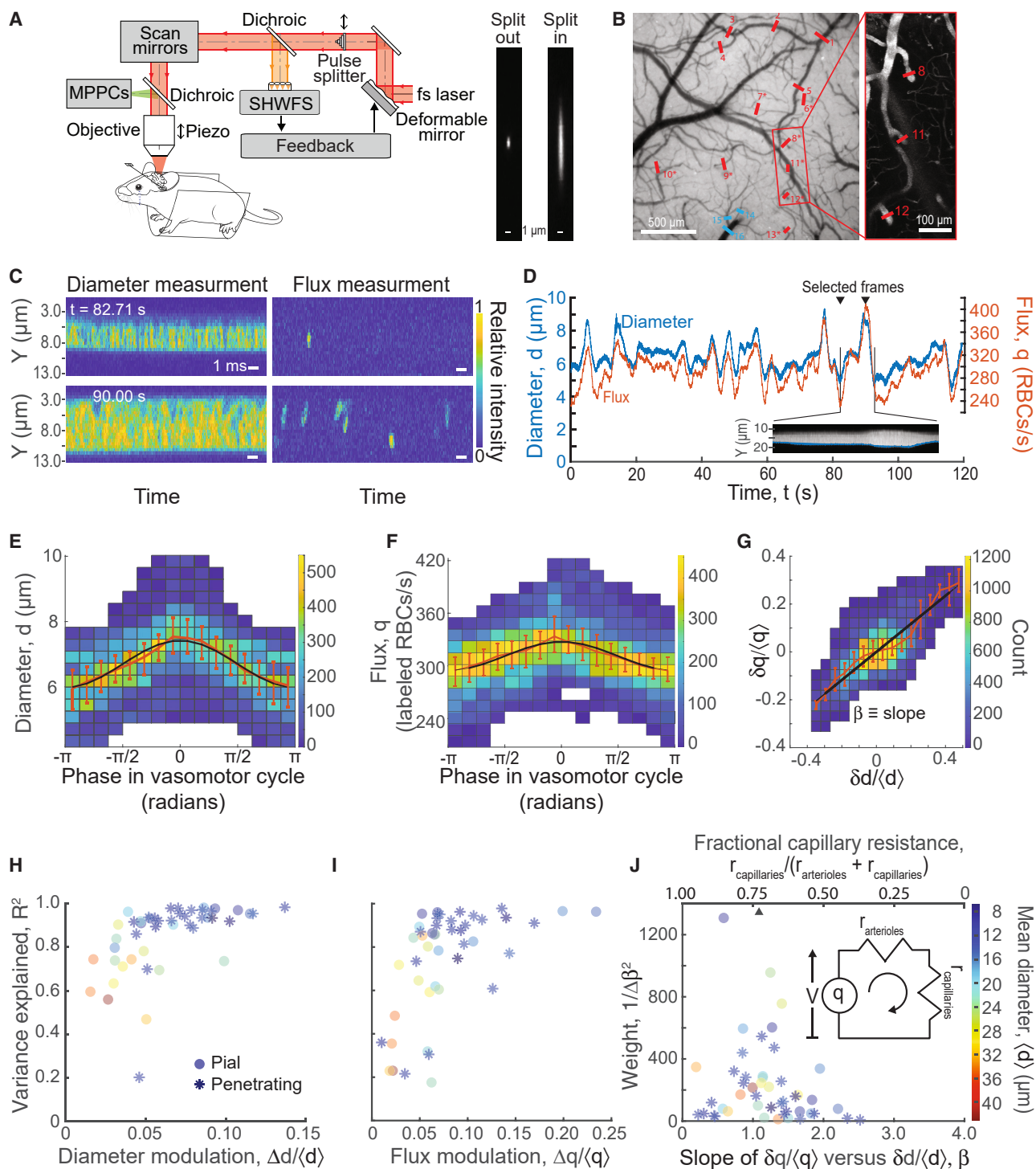
Figure 1. Concurrent measurements of vessel diameter and RBC flux in cortical arterioles

(A) Schematic of the AO-2P microscope with a pulse splitter to extend the axial focus. The inset is the x-z projection of the point-spread function of the regular (Split out) and axially extended (Split in) beam, quantified in Figure S1.

(B) Single-section, widefield image of the surface of cortex to illustrate locations of the "curtain of light" across pial and penetrating vessels. Red lines are across arterioles and blue across venules. Two-photon image of the expanded region to illustrate the position of "curtains" across the surface runs of PAs.

(C) Examples of line scan images (20 ms) of vessel diameter (left) and RBC flux measurements (right) from a "thin skull" preparation. Intensity reports fluorescence from the Cy5.5-labeled vessel lumen (left) and CFSE-labeled RBCs (right).

(legend continued on next page)

Neuron
Article

CellPress

traveling bulge or sinuous variation in diameter, is expected based on the electrotonic properties and electrical excitability of the lumen. Individual smooth muscle cells communicate via gap junctions with the endothelial cells that form the lumen of the vessel.[12] Similarly, neighboring endothelial cells communicate with each other via gap junctions[13] with an electrotonic length constant, the spatial scale in the cable equation, of 1.8–1.9 mm.[14] This results in a net electrotonic coupling among neighboring smooth muscle cells that, in principle, can result in complete synchrony, or in patterns, among arteriole oscillators across the brain. The simplest of such patterns, expected when the coupling among endothelial cells acts to change the timing but not the amplitude of neighboring smooth muscle oscillators, is standing or traveling waves of vasoconstriction along the pial arterioles.[15] Endothelial cells also support active propagation. The fastest pulses involve hyperpolarizing currents,[16,17] with a speed of ~2 mm/s, that can drive constriction and dilation of the muscle cells along an arteriole. Slower currents involve TRP1A receptors and the propagation of Ca^{2+} pulses at ~0.2 mm/s[18]

Here, we examine arteriole vasomotor dynamics and blood flow at the level of individual arterioles, as opposed to areal dynamics across the mantle, with a focus on the resting state of awake mice. We ask: (1) what are the periodic changes in diameter of cortical arterioles? Past work established that the diameter of pial arterioles oscillates during resting-state conditions[8,9,19,20] and, in early measurements, that the fractional change in diameter is ~0.2.[20] Measurements on PAs are unreported. (2) What are the periodic changes in the flux of red blood cells (RBCs) through cortical arterioles? These measurements determine the extent to which vasomotor oscillations modulate the perfusion of cortex. Past data, based on inference from laser Doppler probes and changes in speed of RBCs in capillaries, provide only indirect and qualitative support for a change in perfusion. (3) Do the arterioles or the capillary bed dominate the hydrodynamic resistance of cortical vasculature? The conclusions of modeling studies of flow through the cortical vasculature connectome[21] are equivocal on this issue. Some conclude that the capillary network comprises the dominant resistance to flow[22,23]; thus, the change in flux through PAs over each vasomotor cycle could be negligible. Others predict an increase in

perfusion secondary to vasomotor constriction.[24–26] (4) Do pial arterioles support propagating mechanical waves and, if so, with what spatial frequencies? Prior data indicate traveling waves over short distances, ~0.3 mm, in mice,[27] albeit with methodological uncertainty. (5) Do PAs support propagating mechanical waves, and if so, does propagation enter or exit cortex? Prior measurements of stimulus induced[28] changes in vascular diameter suggest a monotonic propagation out of cortex.[29] Wave motion in PAs is one of several mechanisms that is conjectured to be a prerequisite to peristalsis of perivascular solutes.[30–32] (6) To the extent that traveling waves are observed, what are their relation to the underlying neuronal activity?

RESULTS

Our observations make use of both wild-type and transgenic mice of both sexes that were habituated to head fixation (Figure 1A). The change in diameter of a vessel, denoted d, is parameterized as

$$d(t) = \langle d \rangle + \Delta d \cos\phi(t) \qquad \text{(Equation 1)}$$

where $\langle d \rangle$ is the mean diameter, Δd is the amplitude of the change in diameter over one vasomotor cycle, and $\phi(t)$ is the phase of the vasomotion within a cycle. We explicitly considered only the first Fourier component of the oscillation. The fractional peak-to-peak change in diameter over one cycle is $2\Delta d/\langle d \rangle$. A similar expression holds for the flux of RBCs through a vessel, denoted by q, i.e.,

$$q(t) = \langle q \rangle + \Delta q \cos\phi(t) \qquad \text{(Equation 2)}$$

Vasomotor impact on perfusion of cortex

Technological advances are key to these measurements. We used a thinned skull preparation to insure that vasomotion was not impaired or altered as can occur with a craniotomy.[33] We used two-photon microscopy that incorporated adaptive optics (AO-2P) to correct for distortions caused by strong changes in optical index between blood vessels and tissue[34] (Figure 1A). We added a pulse splitter to the excitation pathway to elongate, but not appreciably broaden, the focus[35] (Figure S1 with splitter

---

(D) Time series of vessel diameter (blue) and RBC flux (orange) measurements in one acquisition section (120 s). Inset: selected vessel line scan image from 80.31 s to 92.80 s.

(E) Joint distribution of the diameter versus the phase of the diameter of a pial artery. Diameter measurements are binned according to their phase to compute the median and 25th and 75th percentiles (error bars). The median diameter in each bin is used to fit Equation 1. The fitting has $R^2 = 0.97$ and normalized modulation depth $\Delta d/\langle d \rangle = 0.11$.

(F) Joint distribution of the RBC flux versus the phase of the diameter of a pial artery. Flux measurements are binned according to their phase for computing the median and 25th and 75th percentiles. The median flux of labeled cells in each bin is used to fit Equation 2. The fitting has $R^2 = 0.95$ and normalized modulation depth $\Delta q/\langle q \rangle = 0.052$.

(G) Joint distribution of normalized change in flux ($\Delta q/\langle q \rangle$) and normalized change in diameter ($\Delta d/\langle d \rangle$). Flux changes are binned according to diameter changes for computing the median and 25th and 75th percentiles. The median flux in each bin is used for linear regression (Equation 3). The fitting has $R^2 = 0.96$ and slope 0.59.

(H) Scatterplot of the diameter modulation depth versus variance explained by the phase-modulation fitting illustrated in (E). Pial and penetrating arteries are shown with color-coded average vessel diameter. The R^2-weighted averages, here and in (I), are in Table 1.

(I) Scatterplot of the flux modulation depth versus variance explained by the phase-modulation fitting illustrated in (F). Pial and penetrating arteries are shown with color-coded average vessel diameter.

(J) Scatterplot of the normalized flux-diameter slope versus the slope's inverse variance-weighting factor. Pial and penetrating arteries are shown with color-coded average vessel diameter. The weighted average slope for pial arterioles, $\beta = 1.09$, is marked with a triangle; values for both pial arterioles and PAs are given in Table 1. The analysis of the model is explained in the text.

in) and a resonant galvo-mirror to scan perpendicular to the axis of the vessel and form a "curtain of light" (Figure 1A). The sharp lateral edge of the focus, in conjunction with labeling of the blood plasma with the far-red fluorescent dye Cy 5.5, provided a means for precise measurements of the change in diameter of surface arterioles (Figures 1B and 1C). The "curtain," in conjunction with low density of RBCs that were harvested from littermates and labeled with CellTrace, provided a means to count passing RBCs for simultaneous measurements of the relative flux through the vessel (Figures 1B and 1C). These datasets made use of wild-type mice (47 trials in 4 mice). The measurements for PAs utilized a short segment along the subarachnoid space that precedes the plunge of the vessel into cortex[36] (Figure 1B).

Qualitatively, we observed changes in flux that largely track concurrent changes in diameter (Figure 1D). The correlation coefficient was 0.72 ± 0.02 (mean ± SEM), and there was a slight lag, 0.16 ± 0.04 s (mean ± SEM) or one-sixtieth of a vasomotor cycle, with changes in diameter leading those in flux (Figure S2A). The specific dependence of changes in diameter relative to phase in the vasomotor cycle was found from an extraction of each cycle by a Hilbert transform of the diameter data.[37] Example data across one vessel, plotted as a two-dimensional histogram, illustrated the changes in diameter (Figure 1E) and flux (Figure 1F) with respect to phase in the vasomotor cycle. For both pial arterioles and PAs, we observed a fractional increase in the flux of RBCs concurrent with the peak of vasomotion.

The distribution of $\Delta d/\langle d \rangle$ across all samples, plotted with respect to the variance explained, i.e., R^2, was distributed between 0.02 and 0.12 for pial arterioles and the slightly narrower range 0.05–0.13 for PAs (Figure 1H; scatterplots of all data are shown in Figures S2B–S2G). In terms of an R^2-weighted average, we found a peak-to-peak change of $2\Delta d/\langle d \rangle \sim 0.11$ for pial arterioles and ~ 0.15 for PAs; mean values and their standard deviations (SD), which report the width of the distribution of values, are listed in Table 1 along with the sample sizes used to compute significance. The values are smaller than those reported by Drew et al.[20] (Table 1) since the analysis in the prior work reported peak changes, whereas here we calculated average changes. Lastly, for the case of periodic vibrissa stimulation at the 0.1 Hz ultra-low frequency of vasomotion, we found a peak-to-peak change of $2\Delta d/\langle d \rangle \sim 0.07$ for pial arterioles and ~ 0.10 for PAs (Figure S3; Table 1).

The change in flux of blood into the parenchyma that accompanies vasomotion was broadly distributed (Figure 1I; Table 1). In terms of an R^2-weighted average, we found that the flux for pial arterioles was modulated with $2\Delta q/\langle q \rangle \sim 0.15$ and for PAs was modulated with $2\Delta q/\langle q \rangle \sim 0.19$. Thus, vasomotion led to a seemingly large cycling in the volume of nutrients available to the brain. Lastly, for the case of ultra-low-frequency vibrissa stimulation, we found a peak-to-peak change of $2\Delta q/\langle q \rangle \sim 0.09$ for pial arterioles and ~ 0.14 for PAs (Figure S3; Table 1).

Hydrodynamic network resistance

Flux and diameter are related through Ohm's law for flow, i.e., $q = P \div R(d)$, where R is the hydrodynamic resistance of the vascular network sourced by the vessel and P is the pressure drop relative to the outflow of the network. Using the form $R \sim d^{-\beta}$, we have

$$\frac{\delta q(t)}{\langle q \rangle} = \beta \frac{\delta d(t)}{\langle d \rangle} + \frac{\Delta P}{\langle P \rangle}. \qquad \text{(Equation 3)}$$

The exponent should vary between $\beta = 4$ for an open pipe and $\beta \to 0$ as the hydrodynamic resistance of the underlying network asymptotes to infinity.

Our concurrent measurements (Figures 1C and 1D) permitted us to estimate the change in flux relative to the change in diameter across all phases on a per-trial basis. We found that the scaling of the resistance, in terms of a variance-weighted average, was $\beta \sim 1.1$ for both pial arterioles and PAs (Figures 1G–1J; Table 1), with an intercept whose mean value was equal to zero within statistics, i.e., $\Delta P/\langle P \rangle = 0.003$ ($p = 0.11$; Table 1).

As a first extension to explore potential systematic contributions to this result, we tested whether the value of β is changed for the case of ultra-low-frequency vibrissa stimulation (30 trials in a subset of 3 mice) (Figure S3). We found, as a variance-weighted average, $\beta \sim 1.1$ for pial arterioles and $\beta \sim 1.3$ for PAs, with an intercept of $\Delta P/\langle P \rangle = 0$ within statistics ($p = 0.24$ and $p = 0.47$ for pial arterioles and PAs, respectively; Table 1). These mean values were found to be statistically different from the resting-state values ($p = 0.004$ and $p < 1 \times 10^{-27}$ for pial arterioles and PAs, respectively).

As a second extension, we artificially drove a change in diameter of pial vessels with the use of mice that express the red-shifted opsin ReaChR[41] in smooth muscle and pericytes under the PDGFRβ promoter[40,42] (21 trials in 3 mice). The opsin was activated by the same AO-2P beam that scans the vessel (Figures S4A and S4B), with the incident power set to induce a 0.2× reduction in diameter over a period of 5 s, like vasomotion. The constriction will spread to neighboring vessels by passive electrical conduction along the endothelium. We found, as a variance-weighted average, $\beta \sim 1.5$ with an intercept of $\Delta P/\langle P \rangle = 0$ within statistics (Figures S4C and S4D; Table 1). This value of β was significantly larger than the value $\beta = 1.1$ determined under natural conditions ($p < 1 \times 10^{-30}$, two-sample t test) yet still small.

In all cases, the observed value of β was significantly far from the value for an open pipe. We considered a one-loop network with two resistors to interpret this value (inset in Figure 1J; STAR Methods). One resistor represented the pial arterioles, with value $r_{arterioles}$, and the other represented the parenchymal network, predominantly capillaries, with value $r_{capillaries}$. Using the definition of β with $\Delta P/P = 0$ (Equation 3) yielded an expression for the fraction of resistance in the capillaries, i.e.,

$$\frac{r_{capillaries}}{r_{capillaries} + r_{arterioles}} = 1 - \frac{\beta}{4}. \qquad \text{(Equation 4)}$$

The observed value of $\beta = 1.1$ during vasomotion implied $r_{capillaries}/(r_{capillaries} + r_{arterioles}) = 0.73$ while the driven value of $\beta = 1.5$ yielded $r_{capillaries}/(r_{capillaries} + r_{arterioles}) = 0.63$. We concluded that the bulk of the hydrodynamic resistance of neocortex lies in the capillary bed and not in supply arterioles.

Table 1. Measured vasodynamic parameters

	Change in diameter, $2\frac{\Delta d}{\langle d \rangle}$ or peak to trough	Change in flux, $2\frac{\Delta q}{\langle q \rangle}$	Slope, β, $\frac{\delta q}{\langle q \rangle}$ vs. $\frac{\delta d}{\langle d \rangle}$	Intercept $\frac{\Delta P}{\langle P \rangle}$	Gradient, $\|k\|$ (radians/mm)	Wave speed, c (mm/s)	Reference method
	mean ± SD	mean ± SD	mean ± SD	mean ± SD	mean ± SD	mean ± SE	
Resting state							
Pial (vasomotor)	0.11 ± 0.06 (n = 24)	0.15 ± 0.11 (")	1.09 ± 0.44 (")	(3 ± 12) × 10⁻³ (")	–	–	This work[a,b] AO-2P
	–	–	–	–	0.33 ± 0.22 (n = 8,869)	2.16 ± 0.02 (")	This work[a] widefield
	0.23 ± 0.10 (n = 118)	–	–	–	–	–	Drew et al.[20] 2P
	0.04 (n = 3)	–	–	–	–	0.41 ± 0.07 (n = 13)	Munting et al.[27] 2P
	0.04 (n = 3)	–	–	–	–	0.97 ± 0.16 (n = 8)	Munting et al.[27] 2P
Pial (cardiac)	<0.013 ± 0.011 (n = 24)	–	–	–	–	–	This work[c] AO-2P
PA (vasomotor)	0.15 ± 0.05 (surface) (n = 23)	0.19 ± 0.07 (")	1.08 ± 0.35 (")	(2 ± 16) × 10⁻³ (")	–	–	This work[a,b] AO-2P
	0.09 ± 0.02 (shallow) 0.07 ± 0.03 (deep) (n = 146)	–	–	–	0.43 ± 0.51 (")	1.96 ± 0.38 (")	This work[a,b] AO-2P
PV	<0.02 ± 0.01 (shallow) <0.02 ± 0.01 (deep) (n = 21)	–	–	–	–	–	This work[d] AO-2P
PA (cardiac)	<0.013 ± 0.006 (n = 23)	–	–	–	–	–	This work[c] AO-2P
Sensory stimulus drive							
Pial	0.07 ± 0.02 (n = 17)	0.09 ± 0.02 (")	1.13 ± 0.22 (")	(2 ± 5) × 10⁻³ (")	–	–	This work[a,b] AO-2P
	–	–	–	–	0.38 ± 0.20 (n = 413)	1.83 ± 0.11 (")	This work[a] widefield
	0.09 ± 0.06 (punctate) (n = 28)	–	–	–	–	–	Drew et al.[20] 2P
	0.22 ± 0.08 (10 s train) (n = 17)	–	–	–	–	–	Drew et al.[20] 2P
	–	–	–	–	–	2.4 ± 0.5 (n = 17)	Chen et al.[38] widefield

(Continued on next page)

Table 1. *Continued*

	Change in diameter, $2\frac{\Delta d}{\langle d\rangle}$ or peak to trough	Change in flux, $2\frac{\Delta q}{\langle q\rangle}$	Slope, β, $\frac{\delta q}{\langle q\rangle}$ vs. $\frac{\delta d}{\langle d\rangle}$	Intercept $\frac{\Delta P}{\langle P\rangle}$	Gradient, $\|k\|$ (radians/mm)	Wave speed, c (mm/s)	Reference method
	mean ± SD	mean ± SD	mean ± SD	mean ± SD	mean ± SD	mean ± SE	
	–	–	–	–	–	0.35 ± 0.04 (n = 14)	Munting et al.[27] 2P
PA	0.10 ± 0.03 (surface) (n = 13)	0.14 ± 0.05 (")	1.31 ± 0.37 (")	(2 ± 7) × 10⁻³ (")	–	–	This work[a,b] AO-2P
	0.12 ± 0.03 (shallow) 0.11 ± 0.03 (deep) (n = 17)	–	–	–	0.74 ± 0.51 (")	0.99 ± 0.22 (")	This work[a,b] AO-2P
	0.24 ± 0.08 (surface) (n = 26)	–	–	–	–	–	Gao et al.[39] 2P
	0.14 ± 0.08 (shallow) (n = 24)	–	–	–	–	–	Gao et al.[39] 2P
Smooth muscle optogenetic drive							
Pial	0.15 ± 0.12 (n = 13)	–	–	–	–	–	O'Herron et al.[40] 2P
	≤0.2 by design (n = 21)	–	1.49 ± 0.90 (")	(0.2 ± 9.2) × 10⁻³ (")	–	–	This work[b] AO-2P

Referenced values are estimated from available data; the lower value for speed from Munting et al.[27] is estimated from measurements of vessel diameter and the larger value is from measurements of smooth muscle Ca²⁺. Note that Gao et al.[39] used 5th and 95th percentile dilation amplitudes, whereas this work uses a least-squares cosine fit over all cycles to calculate an average peak-to-peak change in diameter. Averaging method in footnotes.

[a]R^2 weighted
[b]Inverse-variance weighted
[c]Upper bound, determined as 2 × (RMS in 5–12 Hz band)
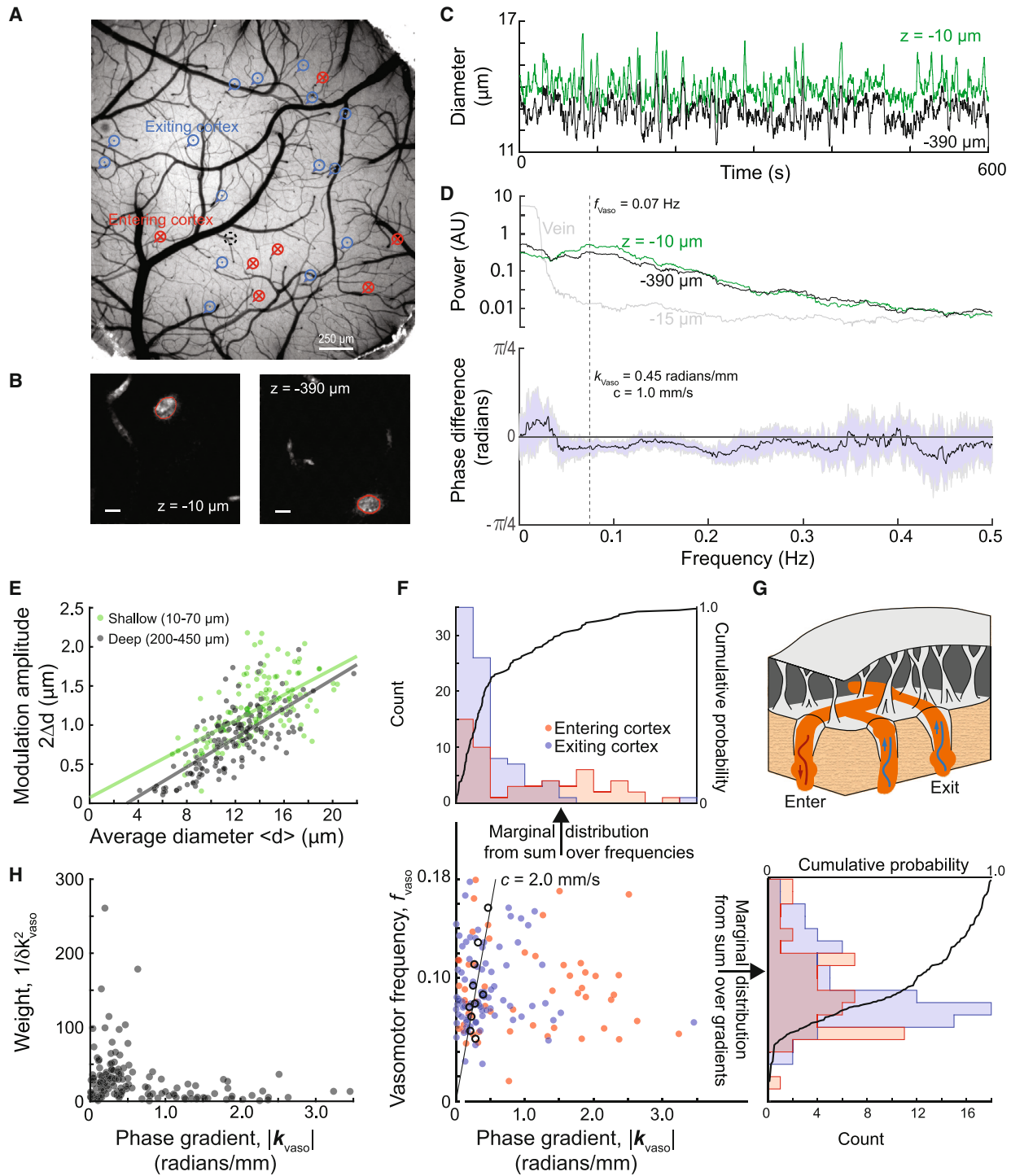[d]Upper bound, determined as 2 × (RMS amplitude in the 0.02 to 0.20 Hz band)

Figure 2. Phase gradients and traveling waves of vasomotion in penetrating arterioles

(A) Example window with measured penetrating vessels labeled. ⊗, measured wave traveling from shallow to deep and entering cortex; ⊙, measured wave traveling from deep to shallow and exiting cortex; ○, penetrating vein. Arrows point directly to the vessel under investigation. Measurement of the marked vessels was performed over two imaging sessions.

(B) Example 2P images and perimeter fits (red) using the Threshold in Radon Space (TiRS)[44] method. Scale bars, 10 μm.

(C) Diameter time traces for vessel cross-sections shown in (B). Here, diameter is the equivalent diameter of a circle with area equal to the region enclosed by the TiRS fits exemplified in (B).

(legend continued on next page)

Cardiac impact on arteriole diameter

Cardiac output modulates the flow of blood in the brain.[43] Does it also modulate the diameter of pial vessels, as has been suggested to support pulsatile pumping of interstitial fluids?[32] We analyzed our data for changes in diameter in the 5–12 Hz spectral band that encompasses the cardiac rhythm (47 trials in 4 mice). We found that the fractional changes, computed as twice the root-mean-square value for comparison with $2\Delta d/\langle d\rangle$, were 0.013 for both pial and PAs (Figure S2H; Table 1). This value serves as a conservative upper bound, given the unresolved contribution of background fluctuations in the spectral window. It is nearly an order of magnitude less than the diameter changes at the vasomotor frequency.

Phase gradients of vasomotion along the PAs

Is the change in diameter synchronous along PAs, or are there differences that could give rise to traveling waves? We examined whether changes in diameter occurred for PAs after they bent and dove from the subarachnoid space into the Virchow-Robin space that surrounds the arterioles in the brain parenchyma (Figure 1B). This requires precision measurements throughout the depth of cortex. We used AO-2P imaging (Figure S1 with splitter out) and a glass window rather than thinned skull to achieve a diffraction-limited focus near the surface and at depths of 450 μm below the pia (Figures 2A and 2B). A piezo-driven translation stage was used to rapidly shift the height of the objective (Figure 1A). We imaged planar fields that encompassed either a diving PA or a penetrating vein (PV) as a control (146 PAs and 21 PVs in 9 mice) (Figures 2A and 2B). The vagaries of vascular anatomy led to shifts in the planar position of PAs at different depths (Figure 2B).

Rhythmic constrictions at the vasomotor frequency were observed at both depths and were coherent across depths (140/146 PAs). The example data in Figure 2C, exhibit a broad vasomotor peak centered at $f_{vaso} \sim 0.07$ Hz. The phase, denoted $\phi(s,t)$, was essentially constant over the ~0.04–0.11 Hz spectral width of this peak (Figure 2D). We calculated the phase gradient, referred to as the spatial frequency in the physical sciences and denoted $\boldsymbol{k}_{vaso}$, as

$$\boldsymbol{k}_{vaso} = \frac{\phi(s,t) - \phi(s - \Delta s, t)}{\Delta s}, \qquad \text{(Equation 5)}$$

where a positive sign of $\boldsymbol{k}_{vaso}$ signifies a propagating bump that enters cortex from the pial surface, a negative sign signifies a

bump that exits the surface, and Δs is the path length between the upper and lower measurements.

As an average over all animals and trials, the fractional change in diameter follows $2\Delta d/\langle d\rangle \sim 0.09$ near the surface and $2\Delta d/\langle d\rangle \sim 0.07$ at depth (Figure 2E; Table 1); the difference is small but statistically significant ($p = 1.3 \times 10^{-19}$, one-tailed paired-sample t test; $p = 4.3 \times 10^{-17}$, one-tailed Wilcoxon signed-rank test). As a control, and unlike in the case of PAs, negligible vasomotion was observed for PVs (Figure 2D; Table 1). For PAs, a phase gradient was observed (Figure 2F). The values of k_{vaso} were broadly distributed with a variance-weighted mean value of $\langle k_{vaso}\rangle \sim 0.43$ radians/mm (Figure 2H; Table 1) or the equivalent wavelength of $2\pi/\langle k_{vaso}\rangle \sim 15$ mm. This corresponds to a weak gradient across the full depth of cortex, estimated as one-eighteenth of a cycle across the thinnest, i.e., 0.80 mm, to one-twelfth of a cycle across the thickest, i.e., 1.2 mm, regions of mouse cortex.[45]

Phase gradients along PAs correspond to traveling waves

The observation of phase gradients along PAs (Figure 2F) suggests the additional possibility of traveling mechanical waves along these vessels. The signature of a traveling wave is a dispersion relation between the frequency and the phase gradient. For linear waves,

$$f_{vaso} = c\,\frac{k_{vaso}}{2\pi}, \qquad \text{(Equation 6)}$$

where c is the speed. The concurrent measurements of vasomotor frequency and phase gradients allowed us to test for traveling waves and estimate their speed. The distribution of data points is broad, reflecting the breadth of the marginal distributions for the frequency as well as the phase gradient (Figure 2F), yet points track one another. The median values across phase gradients in successive frequency bands form a near-linear relation between f_{vaso} and k_{vaso} that is well described by $c = 2.0$ mm/s (Figure 2F; Table 1). Thus, vasomotion corresponded to traveling waves.

Vasomotor waves in PAs travel in both directions, with waves exiting the surface of cortex more often than chance (85 of 140 exit, $p = 0.014$ testing against a binomial distribution with equal probabilities, Figure 2F) and preferentially accounting for large wavelengths (blue dots in Figure 2F center plot). To address possible spatial clustering of the direction of traveling waves across the cortical mantle, we calculated the correlation function for all pairs

---

(D) The spectral power for shallow (green) versus deep (black) measurements of diameters, along with the phase difference ±95% CI. Note the vasomotor peak at both depths. Also shown is the spectral power for a penetrating venule.

(E) The modulation of the diameter for shallow (green) versus deep (black) measurements of diameter as a function of average diameter. Linear fits yield $2\Delta d = 0.08\,\langle d\rangle + 0.07$ ($R^2 = 0.36$) and $2\Delta d = 0.09\,\langle d\rangle - 0.29$ ($R^2 = 0.53$) for shallow vessels and deep vessels, respectively. A straight line fit to all data yields intercept $\langle d\rangle = 2.5$ μm for $\Delta d = 0$ and slope 0.099 ($R^2 = 0.5$, not pictured).

(F) Penetrating arteriole phase gradient versus frequency of vasomotion ($n = 140$) to determine the significance and speed of traveling waves. Entering waves (red) and exiting waves (blue) are indicated in the scatterplots and in the marginal distributions. Each point is one PA, measured for 10 min. The trend was fit to the inverse variance-weighted medians (open circles) across a range of frequencies and all phase gradients. Marginal histograms are the phase gradient (top) and vasomotion frequency (right) distributions, with color separating travel directions; we found a median vasomotion frequency of 0.082 Hz. Cumulative distribution curves incorporate all data, irrespective of travel direction.

(G) Cartoon illustrating our findings.

(H) Statistical weighting of the measured phase gradients across all PAs. Weights correspond to the inverse variance of the phase gradient, $(\delta k_{vaso})^{-2}$, where $\delta k_{vaso}/k_{vaso} = \delta\phi_{vaso}/\phi_{vaso}$ and $\delta\phi_{vaso}$ is determined from leave-one-taper-out jackknife estimates of the phase.
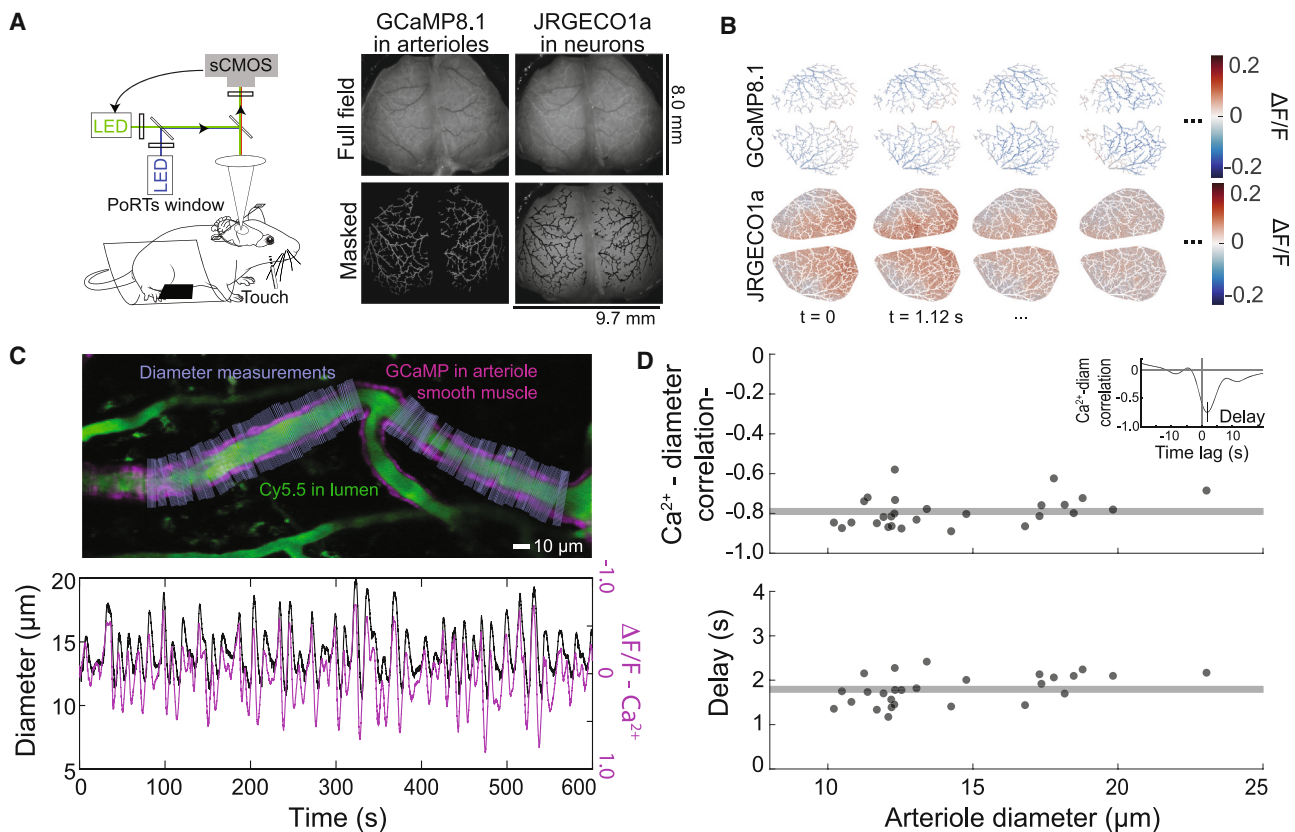
Figure 3. Widefield imaging of the pial arteriole network

(A) Example of a whole-cortex "thin skull" preparation prepared in animals that express GCaMP8.1 in smooth muscle (SMC) or GCaMP8.1 in both SMC and jRGECO1a in excitatory neurons. Rostral is up. Post processing involved generation of a cortical artery mask based on SMC calcium activity. Resting-state experiments were performed with awake animals that were head fixed.

(B) Time series of concurrent one-photon, widefield frames of SMC calcium activity (ΔF/F) in pial vessels and neuronal activity throughout excitatory neurons. False coloring shows that arteriole relaxation (blue) and contraction (red) occurs globally, with various distinct spatial patterns. Similarly, patterns in neuronal activity are observed. Rostral is to the left. Each channel's frame rate is 4.47 Hz, and every 5th frame is plotted.

(C) Example of an AO-2P concurrent measurement of calcium activity along a pial vessel (magenta) and changes in diameter along the same vessel (blue). The blood is labeled with Cy5.5-dextran (green). Diameter is extracted using groups of programmatically defined crosslines. SMC calcium activity is seen to lead to vascular activity. The lower traces represent one trial of data, averaged over all locations along the vessel.

(D) The SMC GCaMP8.1 to diameter delay and peak correlation for 27 pial arterioles measured with AO-2P imaging. Each point is the median value across locations for each vessel. Across vessels, we found an average correlation coefficient of −0.79 ± 0.02 (mean ± SE). The average delay between the peak of the constriction relative to that of the SMC GCaMP8.1 signal is 1.79 ± 0.06 s; there is a slight and statistically significant trend ($p = 0.010$) with delay = 1.093 + 0.049 ⟨d⟩. The average correlation function across all vessels is shown in the inset. The horizontal lines are the mean ± SE values.

of PAs within each imaging session (Figure S5). Propagating waves between pairs of PAs were equally likely to be the same as in opposite direction (cartoon in Figure 2G) ($p = 0.51$, binomial analysis). We concluded that there are no clusters of PAs that, in principle, support net peristaltic pumping along the Virchow-Robin space.

Phase gradients of vasomotion along the pial arterioles

The unique capability of AO-2P to image deep in cortex enabled measurements of phase gradients in PAs. Yet two-photon imaging has limited ability to image across large-distances without a drop in resolution. To study phase gradients along the network of pial arterioles that span the cortical mantle (Figure 1B), we switched to mice that expressed an intracellular calcium indicator in smooth muscle,[27,28,46,47] i.e., GCaMP8.1[48] tied to the acta2 promotor[48] (24 mice) (Figure 3A). Changes in intracellular Ca²⁺

served as a surrogate of arteriole diameter.[49] These mice also expressed the red-shifted intracellular calcium indicator jRGE-CO1a in excitatory neurons; we return to use of this indicator later. The response from the entire mantle was recorded using full-field one-photon imaging[50] (Figure 3B).

Multiple potential systematic errors were addressed. First, the absorption and emission spectrum of GCaMP8.1 overlaps with the absorption spectrum of hemoglobin. Yet arteriole blood is typically 0.99 saturated with oxygen, so systematic errors from changes in brain utilization of oxygen are expected to be negligible. Second, nonlinearities in the coupling of smooth muscle contraction to intracellular calcium[49,51] and a systematic decrease in the observed emission from GCaMP8.1 concurrent with an increase in arteriole diameter can affect the estimate of arteriole diameter. To control for these possibilities, we
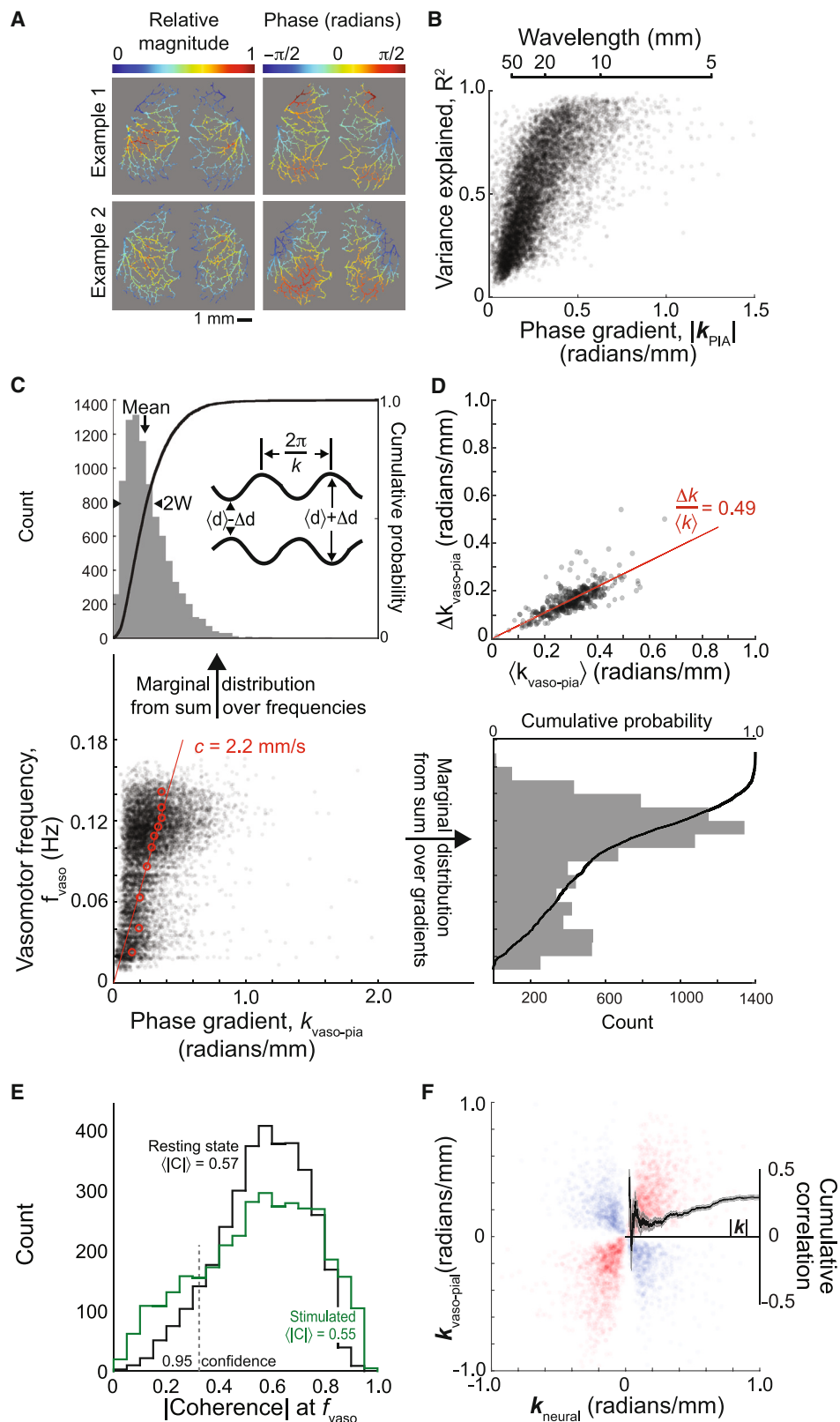
(legend on next page)

established a phenomenological link between the GCaMP8.1 signal and the change in arteriole diameter via concurrent two-photon imaging of the GCaMP8.1 signal and diameter (Figure 1A with pulse splitters in; Figure 3C). This led to a peak correlation of ∼0.8 over the full range of pial arteriole diameters (Figure 3D); the same value was found for the spectral coherence at ∼0.1 Hz, which further indicates that the coherence between Ca^{2+} and mechanical signals is valid up to ∼0.3 Hz (Figures S6A and S6B). Thus, we trade off a slight decrement in reliability of our measurements to gain an increase in length and number of pial vessels in our cohort. The delay from the calcium signal to constriction, as determined from the correlation, was 1.8 s and was independent of arteriole diameter (Figure 3D). The delay may be shorter when measured in terms of onset time (Figure 3C).[28] Yet in all cases, waves observed from Ca^{2+} dynamics were temporally translated versions of the mechanical waves.

To achieve population statistics, we observed the spatial pattern for vasomotion with full-field imaging visualized in terms of the dominant space-frequency mode of the data.[52] This mode corresponds to rhythmic dynamics at the center frequency of vasomotion, denoted f_{vaso}, for each run; two examples are shown in Figure 4A, and the remainder across all datasets are shown in Table S1. A linear fit to the phase at the vasomotor frequency as a function of distance was used to compute the phase gradient, i.e.,

$$\boldsymbol{k}_{vaso} = \frac{\Delta\phi(s.t)}{\Delta s},$$ (Equation 7)

where Δs is the path along the vessel. The detailed pattern of arteriole dilation across the mantle varies between mice in terms of both amplitude and phase (Figure 4A; Table S1). Yet phase gradients of vasomotion along pial arterioles are a common statistical feature (24 mice; 8,869 arterioles; 337 predominantly 500 s trails). We extracted segments longer than 0.75 mm in length across trials and mice and estimated the spatial gradient on an arteriole-by-arteriole basis. The variance explained of the fit versus k_{vaso} showed a broad distribution (Figure 4B) with an R^2-weighted mean of $\langle k_{vaso}\rangle \sim 0.33$ radians/mm (Table 1) or a

typical wavelength of $2\pi/\langle k_{vaso}\rangle \sim 19$ mm, i.e., nearly double the full spatial extent of the murine cortical surface.

Traveling waves along pial arterioles
As in the case of PAs, the concurrent measurements of pairs of vasomotor frequency and phase gradients for arteriole motion allowed us to test for traveling waves. Here, too, the distribution of data points was broad, reflecting the breadth of the marginal distributions for both the frequency and phase gradient, yet their magnitudes tracked each other (Figure 4C). The median values formed a near-linear relation between f_{vaso} and k_{vaso} that is well described by $c = 2.2$ mm/s (Figure 4C; Table 1). Thus, vasomotion in pial vessels also corresponded to traveling waves with relatively long wavelengths (cartoon in Figure 4C).

The marginal distribution of k_{vaso} for pial vessels is necessarily broad, with a half-maximal half-width, W, of 0.12 radians/mm (Figure 4C). What is the variability of the phase within a trial? We found that the SD, denoted $\Delta k_{vaso-pia}$, tracks the mean value, $\langle k_{vaso-pia}\rangle$, with a slope of $\Delta k_{vaso-pia}/\langle k_{vaso-pia}\rangle = 0.49$ (Figure 4D). This implies a relatively high degree of variability in wave propagation on a cycle-by-cycle basis; recall that the fractional uncertainty in the mean values of $k_{vaso-pia}$, measured over the ∼50 cycles of vasomotion in each trial, is only $0.49/\sqrt{50} \sim 0.07$.

Entrainment by cortical neurons
What is the origin of the phase gradients of vasomotor activity? Prior work shows that vasomotion in pial arterioles can phase lock to the underlying neuronal activity in the resting state.[8] Locking is partial, with a composite $R^2 \sim |C|^2$,[19] where $|C|$ is the magnitude of the coherence. The values of R^2 range from 0.1 to 0.3 across optical studies in mice[8,19] and $R^2 \sim 0.1$ between the blood-oxygen-level-dependent (BOLD)-fMRI signal[53] or cerebral-blood-volume (CBV)-fMRI signal[54] and single-electrode measurements in nonhuman primate studies. This suggests that the spatial phase gradients observed in the vasculature can be inherited, in part, from the underlying neuronal activity. To test for phase locking of neuronal and vascular phase gradients at the vasomotor frequency, we utilized the expression of the red

Figure 4. Phase gradients and traveling waves of vasomotion in pial arterioles
(A) Magnitude and phase of the dominant space-frequency SVD mode at the vasomotor frequency for two example resting-state trials obtained from arteriole GCaMP8.1 data with widefield imaging (Figure 3). Rostral is up. Here, delay increases with increasing phase. Hence, in example 2, vasomotor waves travel on a lateral-to-medial and rostral-to-caudal axis on average, whereas in example 1, the pattern is more complicated. Note the restricted range of phase to π rather than 2π; all datasets are in Table S1.
(B) Scatterplot of the variance explained, R^2, in the phase gradient versus the corresponding magnitude of the phase gradient. The sample included 8,869 pial arteriole segments longer than 0.75 mm that pass a phase versus distance fit t test at a confidence level of $\alpha = 0.01$.
(C) Pial arteriole phase gradient versus frequency of vasomotion for all arterioles to determine the significance and speed of traveling waves. Each data point is one pial arteriole. We further show the marginal distributions; we found a median value of 0.105 Hz for the vasomotor frequency. The trend was fit to the R^2-weighted medians (open red circles) across a range of frequencies and all phase gradients. The cartoon illustrates the relationship between phase gradient magnitude $\boldsymbol{k}$ and wavelength. Phase gradient variability, visualized as half-width W (top), sets a scale for which changes in phase can be ignored; this is investigated further in (D).
(D) Scatterplot of trial-wise fractional uncertainty in phase gradient. Because differences across animals and trials may broaden the phase gradient distribution in (C), here variability is assessed within each imaging trial. $\langle k_{vaso-pia}\rangle$ and $\Delta k_{vaso-pia}$ correspond to the intra-trial phase gradient average and standard deviation, respectively. A linear fit through the origin yields a fractional uncertainty of 0.49.
(E) Magnitude coherence between arteriole GCaMP8.1 and neural envelope jRGECO1a signals from vessels in the vibrissa cortex during air puff stimulation experiments (10 mice and 3,518 arterioles; here we include all arterioles regardless of length).
(F) Scatterplot of pial arteriole phase gradient versus neuronal envelope phase gradient. Arterioles whose vessel and neural waves travel in the same direction have same-signed $\boldsymbol{k}_{vaso}$ and $\boldsymbol{k}_{neural}$ (red, 2,354/3,788 arterioles). Here, we consider only arteriole and neural wave pairs that both pass a phase versus distance fit t test at a confidence level of $\alpha = 0.01$. Points with $\boldsymbol{k}_{vaso} = \boldsymbol{k}_{neural}$ represent waves that travel in the same direction with equal speeds. Connected correlation, M (Equation 6), is plotted cumulatively for all $|\boldsymbol{k}| = (k_{neural}^2 + k_{vaso}^2)^{1/2}$. Bootstrap SE is calculated using randomly sampled (k_{neural}, k_{vaso}) pairs and is shown in gray.
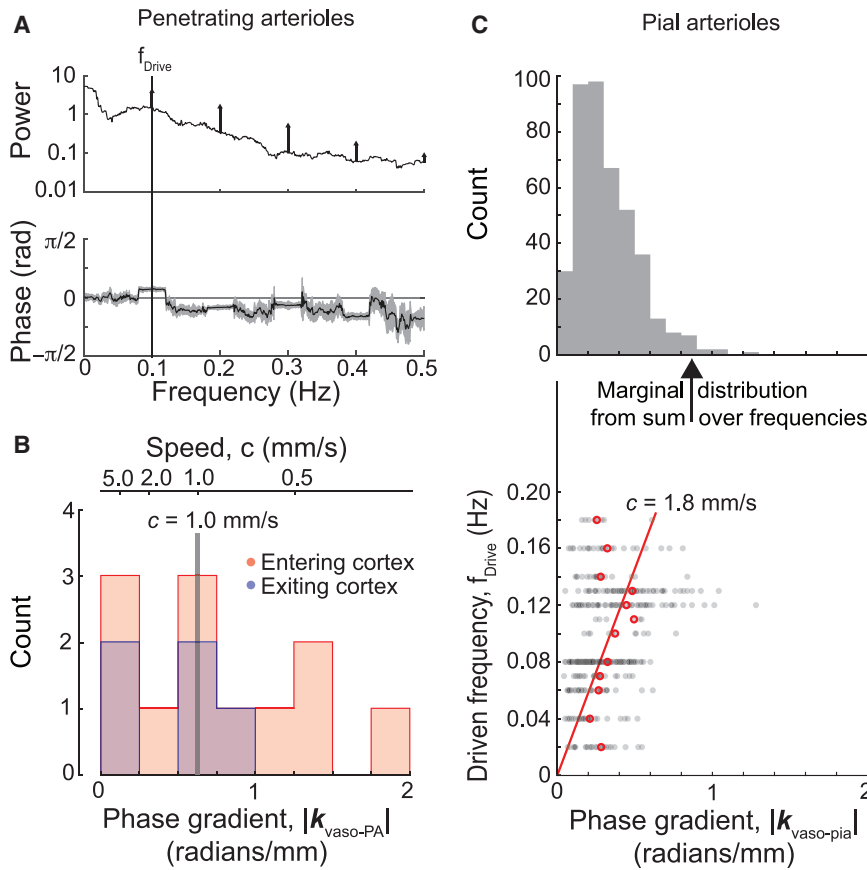
Figure 5. Penetrating and pial arteriole waves in response to stimuli

(A) An example power spectrum for the shallow segment of a PA during 0.1 Hz air puff stimulation (top). Significant periodic diameter changes were detected at the drive frequency and drive-frequency harmonics (vertical arrows). The corresponding phase ± SD between shallow and deep PA segments during 0.1 Hz stimulation is shown on the bottom. The positive phase at the drive frequency indicates a wave that is entering cortex.

(B) Magnitude of the k_{vaso} distribution for PAs during 0.1 Hz air puff stimulation. The $c = 1.0$ mm/s line corresponds to $c = 2\pi(0.1 \text{ Hz})/k_{vaso,med}$ where $k_{vaso,med}$ is the weighted median $|k_{vaso}|$.

(C) Dispersion relation for pial arterioles across the surface of vS1 cortex during air puff stimulation at various frequencies for 413 arterioles longer than 0.75 mm. Linear regression on weighted-median f_{vaso} versus $|k_{vaso}|$ yields $c = 1.8 \pm 0.1$ mm/s. Open red circles are weighted medians of the $|k_{vaso}|$ at each stim frequency (black points).

The first term is the cross-correlation, and the second term subtracts the spurious correlation so that $M = 0$ when k_{neuro} and k_{vaso} are independent random variables. We found that $M = 0.28 \pm 0.02$, from which we again concluded that neural activity has a modest but highly significant influence on pial traveling waves.

We next asked whether waves that are potentially generated by sensory stimuli have a different speed than the natural vasomotor waves. For the case of PAs, we used only a single stimulation frequency, $f_{drive} = 0.1$ Hz, given the complexity of obtaining precision data throughout the depth of cortex (Figure 2). Thus, the observed distribution of k_{drive} with PAs yields the distribution of speeds. We focused on arterioles in the vicinity of vibrissa sensory region (17 trials in 17 vessels and 2 mice) in response to repetitive air puff stimulation of the vibrissae (Figure 5A). At the stimulation frequency, we found that k_{drive} was broadly distributed between 0.1 and 2 radians/mm, with median k_{drive} yielding $c = 1.0$ mm/s (Figure 5B). We further observed waves that traveled in both directions, with waves exiting and entering the field of view at chance (12 of 17 enter, $p = 0.14$) (Figure 5B). For pial vessels, we readily obtained a large dataset over a range of stimulation frequencies. At the stimulation frequency using median values on k_{drive}, we found that $c = 1.8$ mm/s (Figure 5C), close in value albeit statistically smaller than the value under resting state ($p = 0.0034$, one-tailed test) (cf. Figures 4C and 5C; Table 1). All told, the combined data for the resting-state and stimulated data imply that the wave speed for cortical arterioles clocks in at ~2 mm/s.

A final control serves to validate the inference of vasodynamics from neural activity, in which calcium activity in smooth muscle cells serves as a surrogate of vessel diameter (Figure 3) and neuronal calcium transients serve as a proxy for electrical spikes.[55] Here, we used the Graph-Filtered Temporal Dictionary procedure[56] to predict the full-field vascular response from that

calcium indicator jRGECO1a in all excitatory neurons in addition to the green indicator GCaMP8.1 in smooth muscles (Figure 3A) and extended the widefield imaging to two colors of excitation light (Figure 3B). Note that emission from jRGECO1a and GCaMP8.1 are spectrally separate.

As an average over all arterioles in the vibrissa sensory region (96 trials in 3,518 vessels and 10 mice), we observed that the coherence between vessels and neurons is significant both during the resting state and in response to air puff stimulation of the vibrissa (Figure 4E). The measured magnitude of the coherence is $|C| \sim 0.57$, consistent with previous reports of the coherence between changes in arteriole diameter and the electrocorticogram (ECoG).[8] The distribution of coherences for the vibrissa region is slightly, albeit significantly shifted with stimulation ($p = 6.7 \times 10^{-16}$, two-sided Kolmogorov-Smirnov test) (Figure 4E), again consistent with past measurements of coherence.[8]

As a specific test of the influence of neuronal activity on phase gradients along vessels, we plotted the estimate of k_{vaso} from the pial arterioles against the estimate of k_{neuro} from the underlying neurons (Figure 4F). We determined k_{neuro} from the neuronal activity along strips that bordered the arterioles (Figure S6C). To quantify the extent of neural influence on vessel traveling waves, we calculated the connected correlation, denoted M with $-1 \leq M \leq 1$ and

$$M = \frac{<k_{neuro} \cdot k_{vaso}> - <k_{neuro}> \cdot <k_{vaso}>}{\sqrt{<k_{neuro}^2><k_{vaso}^2>}}.$$
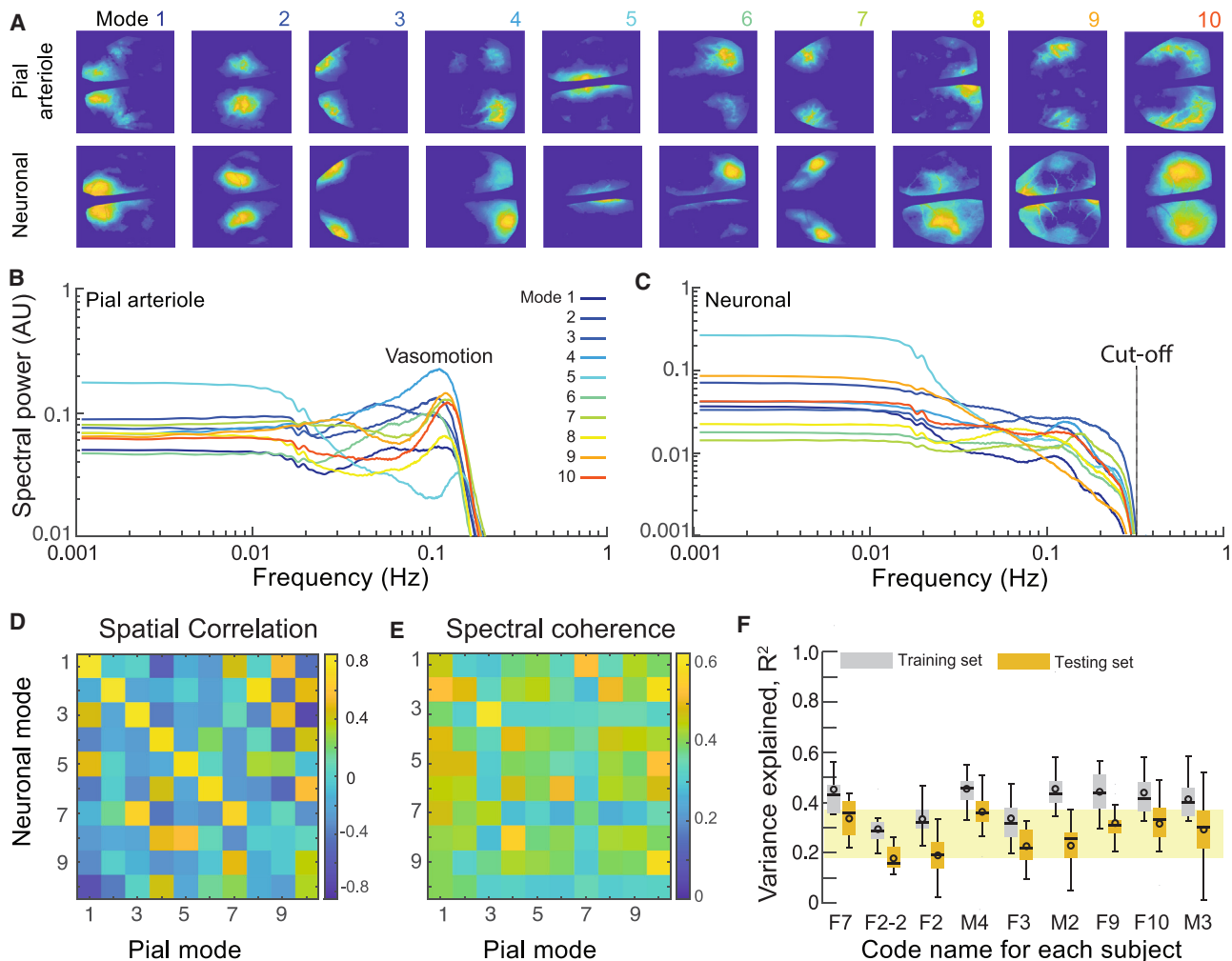(Equation 8)

Figure 6. Modal analysis of the resting-state response

(A) Pial arteriole spatial modes (top) and neuronal spatial modes (bottom) from the GraFT decomposition. The modes are nominally matched with decreasing spatial correlation. Data from mouse M4 (48 trials) (F). The neuronal data were low-pass filtered to match the 0.22 Hz high-frequency fall-off of the vasomotor data (B).

(B) Spectra of the first ten temporal, i.e., dictionary modes for the pial vessels for the dataset in (A). Note the peak near 0.1 Hz. Half-bandwidth = 0.02 Hz.

(C) Spectra of the first ten temporal, a.k.a. dictionary modes for the neurons for the dataset in (A). Half-bandwidth = 0.02 Hz.

(D) Pairwise spatial correlation matrix between the neuronal and pial arteriole spatial modes.

(E) Pairwise spectral coherence matrix between the neuronal and pial arteriole temporal modes.

(F) Boxplots of training and test R^2 scores across 9 mice. In each box, the center mark indicates the median, the center dot indicates the mean, the top and bottom edges of the box indicate the 25th and 75th percentile, and single dots are outliers, which are 1.5 or more times the interquartile range from the median. The whiskers extend to the most extreme data points that are not outliers. The light-yellow band indicates the R^2 range within 1 SD with respect to the mean of all the testing set results.

of the underlying neurons. This procedure uses a graph-regularized dictionary-learning-decomposition in which the datasets are expressed in modes for further analysis, as illustrated for repeated trials across one mouse in Figure 6A. The spectra for the pial arteriole modes all showed a vasomotor peak, except for a single mode in cingulate cortex (mode 5, Figure 6B). In contrast, and as expected, the spectra for the neuronal responses were broadband (Figure 6C). The independently derived vascular and neuronal spatial modes largely coincided on a pairwise basis (Figure 6A). Further, many spatial modes, e.g., pial modes 1, 3, 4, 7, and 10, were correlated with multiple neuronal

spatial modes (Figure 6D). Nonetheless, the accompanying temporal modes may be only weakly coherent between vessels and neurons, e.g., mode 7 (Figure 6E). As a summary across all animals (231 datasets across 9 mice), predicting pixel-wise time traces for the vascular responses based on the extracted temporal modes of the neuronal responses resulted in $R^2 \sim 0.2$ to 0.4 for the test sets (Figure 6F). In total, the distribution across all trials and mice yielded $R^2 = 0.28 \pm 0.10$ (mean ± SD). This is similar to measurements at a single location.[8] As expected for correlations, the inverse model of predicting neuronal responses from pial responses yielded equivalent values (Figure S7).
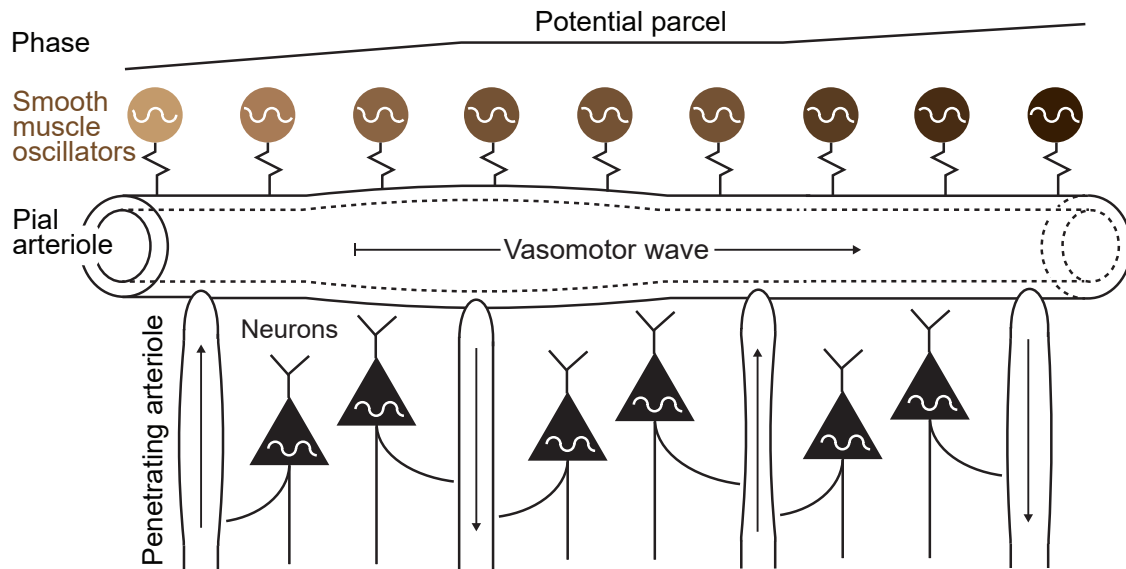
Figure 7. Model of pial and penetrating vessel traveling waves
The observed vasodynamics are influenced by both ongoing neuronal activity and neighboring smooth muscle cell oscillators. Vascular phase, partially driven by neural activity, progresses over millimeter scales but is variable on shorter length scales to potentially form constant-phase parcels.

DISCUSSION

Vasomotion is a dominant feature of vascular dynamics[1,19,57–60] and a dominant feature of resting-state fMRI signals,[61,62] particularly those used to define functional connectivity.[63,64] Further, past work has shown that vasomotion is partially entrained by the local neuronal activity.[8] Critically, the timing of vasomotion across mirrored regions of the two hemispheres is dependent on callosal projections[8,65] so that correlations in the fMRI signal at the vasomotor frequency are a measure of functional connectivity among brain regions. Yet, despite the prevalence and importance of vasomotion (Figure 7), essential questions remained as to the strength and dynamics of this physiological effect.

We show that vasomotion modulates the flux of blood into cortex by a factor of 0.19 ± 0.07 over the course of the approximately 10 s vasomotor cycle (Figures 1F–1I; Table 1). This compares with a relative change in flux of 0.14 ± 0.05 in vibrissa cortex in response to stimulation (Figure S3; Table 1). This directly measured value may be compared with estimates from prior indirect measurements of flux in neocortex. A fractional change of 0.17 in flux through PAs in anesthetized rats is estimated from single-vessel CBV-fMRI data.[66] Changes of ~0.11 for awake mice,[67] 0.20 ± 0.06[68] and ~0.20[67] for anesthetized mice, and 0.23 ± 0.04 for anesthetized rat[69] are estimated under the assumption that the increase in capillary flux must follow the increase in PA flux. Thus, the change in perfusion of cortex over a vasomotor cycle during the resting state is somewhat larger in magnitude, ~0.2, than that following sensory stimulation in the awake animal. To the extent that functional hyperemia is believed to satisfy a need for increased nutrients in a brain area, it remains to be determined whether aspects of cognition vary across the vasomotor cycle.

While vasomotion leads to a cyclic variation in the flux of blood into cortex, a traveling bulge leads to an additional change. We expect a net increase in flux through the PA for entering waves and a net decrease for existing waves. How big is this effect? The fractional change in flux, denoted $\Delta q_{wave}/\langle q \rangle$, can be *crude*ly estimated by assuming that the traveling mechanical bulge transports additional blood. We estimate

$$\frac{\langle \Delta q_{wave} \rangle}{\langle q \rangle} \approx \frac{2\pi \int_0^{2\pi/k} dx \int_{(\langle d \rangle - \Delta d)/2}^{(\langle d \rangle - \Delta d \cos kx)/2} r\,dr}{\pi \left(\frac{\langle d \rangle}{2}\right)^2 \frac{2\pi}{k}} \frac{\frac{c\,k}{2\pi}}{\frac{\langle v_{PA} \rangle\,k}{2\pi}} \xrightarrow{\frac{\Delta d}{\langle d \rangle} \ll 1} \frac{\Delta d}{\langle d \rangle} \frac{c}{\langle v_{PA} \rangle}$$

(Equation 9)

where $\langle v_{PA} \rangle$ is the average RBC speed through a PA. The integral of the pumping volume, in cylindrical coordinates, is taken along the full length of the bulge to maximize the estimate of additional transport. The integral is readily solved, but since the modulation of the PA diameter is small, we expand the solution to first approximation to gain insight into the dependence on the different parameters. Using the data of Table 1 and $\langle v_{PA} \rangle \sim$ 8 mm/s,[70] the fractional change in perfusion is $\Delta q_{net}/\langle q \rangle \sim$ 0.02, which is an order of magnitude less than the cyclic variation in flux of $\Delta q/\langle q \rangle$ (Table 1). Thus, we estimate that the magnitude and direction of wave motion has an effect, albeit small, on the perfusion of blood into cortex.

The measured relation between changes in flux and arteriole diameter, i.e., the slope $\beta \sim 1.1$ (Figures 1G–1J), implies a high resistance of the vascular bed downstream of the PAs. The precise interpretation of the value of β depends on details of a network model, much like that for current flow in a power grid,[71] and on the spatial extent of the vasodilation at the pia. Nonetheless, the analysis of a minimal model, with one resistor

modeling the arteriole and one resistor modeling the capillary network (inset in Figure 1J), which dominates the resistance of the downstream vasculature, implies that the capillaries provide 0.7 of the total resistance. This may be compared to 0.85 ± 0.06 for resistance-based numerical simulations[22] and 0.52 for simulations based on tracking of RBCs through individual capillaries.[23] All told, the accumulated present and past evidence supports the conclusion that the majority of hydraulic resistance lies within the capillary bed and not in the pial and penetrating arterioles.[22,28]

Unification of data on the speed of propagation

We observed wave speeds of ~2 mm/s, albeit slower for stimulus-induced propagation in PAs (Figures 2F, 4C, 5B, and 5C; Table 1), under normal physiological conditions. An upper bound on the mechanical wave speed is expected to be set by active electrical propagation in endothelial cells, with a speed of ~2 mm/s[16,17] This value could increase with hyperthermia as the frequency of vasomotion increases with temperature.[3,72] Yet, it is surprising that the observed mechanical speed corresponds to the speed of active propagation since the latter depends on a high level of extracellular potassium to activate the inward rectifier channel.[16] Perhaps passive propagation supports a front with a similar speed.[73] Our measurements provide post hoc support for the interpretation of a propagating front of oxygenation in the parenchyma after sensory stimulation, with a speed 2.5 ± 0.5 mm/s (mean ± SE), as a pial wave.[38] They supplant prior claims[27] of propagation speeds of 0.4–1.0 mm/s that were apparently confounded by short vessel lengths (Figure S8).

Relation of waves to peristalsis

It has been proposed that coordinated waves along PAs could support transport of interstitial solutes by peristalsis.[30,74–77] We found that there is only a slight bias to the direction of wave propagation (Figure 2F) and that neighboring PAs are nearly as likely to have waves entering cortex as exiting (Figure S5). Nonetheless, potential peristaltic waves could still churn cerebrospinal fluid (CSF) and prevent buildup of denatured proteins, consistent with evidence that increased vasomotion supports increased clearance of solutes during wakefulness[31,78] and, albeit debatably, sleep.[79–82]

We estimated an upper bound for local peristaltic flow by assuming that the wall of the Virchow-Robin space is relatively stiff and impermeant, so as the PA dilates, it presses against the wall and can trap CSF that is then pumped in the direction of the traveling wave. The average volume of CSF pumped on each vasomotor cycle, denoted $\langle \Delta V_{pump} \rangle$, may be readily estimated if we capitalize on the relatively high impedance of the capillary network sourced by the PAs (Figure 1J) and further assume that the brain tissue is stiff to achieve maximum pumping.[83] Lastly, we normalize to the cylindrical volume of tissue that surrounds the PA, denoted $\langle V_{PA} \rangle$. Thus,

$$\frac{\langle \Delta V_{pump} \rangle}{\langle V_{PA} \rangle} \approx \frac{2\pi \int_0^L dx \int_{(\langle d \rangle + \Delta d \cos kx)/2}^{(\langle d \rangle + \Delta d)/2} r dr}{\eta \pi \left(\frac{D_{PA}}{2}\right)^2 L} \xrightarrow[\frac{\Delta d}{\langle d \rangle} \ll 1; \, kL \ll 1]{} \frac{1}{3\eta} \frac{\Delta d}{\langle d \rangle} \left(\frac{\langle d \rangle}{D_{PA}}\right)^2 (kL)^2$$

(Equation 10)

where L is the thickness of neocortex, η is the fraction of parenchyma that is extracellular space, and D_{PA} is the distance between PAs. The integral of the pumping volume, in cylindrical coordinates, is taken along the PA with a length L and diameters that capture the maximum volume, i.e., the choice of maximal diameter at the surface. The integral is readily solved, but since the modulation of the PA diameter is small and $kL \ll 1$, we expanded the solution to first approximation to gain insight into the dependence on the different parameters (Equation 10). For our estimates of $\Delta d/\langle d \rangle$ and k (Table 1), along with $L \sim$ 1 mm,[45] $\eta = 0.2$,[84] and $D_{PA} \sim 120$ μm,[21] we found that $\langle \Delta V_{pump} \rangle / \langle V_{PA} \rangle \sim 3 \times 10^{-4}$. The time to transport this volume of fluid is given by $(1/f_{vaso}) \langle V_{PA} \rangle / \langle \Delta V_{pump} \rangle \sim 3 \times 10^4$ s $\sim$ 1/2 day. All told, our estimate suggests that it is unlikely that peristalsis from a traveling bulge contributes to the net transport of solutes, although the enhanced mixing of solutes may serve a diurnal physiological role.[79] Of course, PAs with anomalously large phase gradients could have an outsized impact on fluid transport, albeit large gradients are associated with waves entering cortex (Figures 2F and 5B). Peristaltic vasomotor waves may also facilitate solute movement through alternate routes, such as the intramural periarterial drainage pathway.[74,85] Independent of the validity of our model (Equation 10), measured vasomotor parameters (Table 1) are crucial to future models that clarify physiological contributions to solute clearance.

Epilogue

The wavelength of the observed pial waves is long, typically 20 mm or twice the length of the mouse cortex (inset in Figure 4C). Thus, vasomotion across a given functional region of mouse cortex is relatively uniform and should not perturb the distribution of new blood. We estimate the SD of the spatial localization of the bulge in pial arterioles as

$$\Delta x \approx \Delta \left(\frac{2\pi}{k_{vaso}}\right) = \left(\frac{2\pi}{k_{vaso}}\right) \frac{\Delta k_{vaso}}{k_{vaso}}.$$ (Equation 11)

Using our experimental values (Table 1), we found that $\Delta x = 9$ mm; of course, averaging over time improves the estimate of the centroid of activity. Thus, the long wavelength of the phase gradient (Figure 4B), the broad distribution of the gradient (Figures 2F and 4B), the associated variability of the gradient (Figures 4D and S8C), and the estimate of Equation 11 all support the viability of a uniform phase within a restricted region of neocortex (potential parcel in Figure 7). This claim is consistent with the notion of parcellation of vasomotion that is used to interpret fMRI datasets.[86–88]

As a practical issue, the direction of the waves is tied, albeit weakly, to the underlying neuronal activity (Figure 4F). Thus, a challenge is to use vasodynamics in the decoding of fMRI signals, particularly the CBV-fMRI signal as this is selective for arterioles. While contributions from the heart appear to have a minimal role in modulating brain blood flow (Table 1), they and other confounds may influence fMRI signals.[89,90]

A final conjecture is that phase gradients and the associated waves may serve to spread disturbances in vasomotion, such as those that result from local changes in the mean hydrodynamic resistance of vessels as occurs through autoregulation.[91,92] This

CellPress

Neuron
Article

could minimize the buildup of pressure gradients and corresponding regions of low perfusion or profoundly high perfusion.

STAR★METHODS

Detailed methods are provided in the online version of this paper and include the following:

- KEY RESOURCES TABLE
- RESOURCE AVAILABILITY
  - Lead contact
  - Materials availability
  - Data and code availability
- EXPERIMENTAL MODEL AND STUDY PARTICIPANT DETAILS
  - Experimental subjects
- METHOD DETAILS
  - Common surgical procedures
  - Common post-surgical preparation
  - Simultaneous diameter and flux measurements
  - Penetrating vessel diameter measurements
  - Penetrating vessel diameter extraction
  - Penetrating vessel spectral analysis
  - Travel direction spatial correlation calculation
  - Simultaneous AO-2P measurements of smooth muscle calcium and arteriole diameter
  - Simultaneous widefield measurements of pial arterioles and cortical neurons
  - Mask creation and dF/F calculation from widefield data
  - Phase-gradient calculation from widefield data
  - Stimulation paradigms
- QUANTIFICATION AND STATISTICAL ANALYSIS
  - Spectral methods
  - Resting state spectral estimation from widefield data
  - Spectral estimation for PAs during periodic stimulation
  - Propagation analysis
  - Weighted averages and significance tests
  - Vessel length and estimated speed
  - Resistance model
  - Modal areal analysis
  - Graph-Filtered Temporal Dictionary (GraFT) procedure
  - Spatial correlation
  - Spectral coherence
  - Linear prediction analysis
  - Code

SUPPLEMENTAL INFORMATION

Supplemental information can be found online at https://doi.org/10.1016/j.neuron.2024.04.034.

REFERENCES

1. Intaglietta, M. (1990). Vasomotion and flowmotion: Physiological mechanisms and clinical evidence. Reviews in Vascular Medicine *1*, 101–112.

2. Haddock, R.E., and Hill, C.E. (2005). Rhythmicity in arterial smooth muscle. J. Physiol. *566*, 645–656.

3. Osol, G., and Halpern, W. (1988). Spontaneous vasomotion in pressurized cerebral arteries from genetically hypertensive rats. Am. J. Physiol. *254*, 28–33.

4. Kontos, H.A., Wei, E.P., Navari, R.M., Levasseur, J.E., Rosenblum, W.I., and Patterson, J.L., Jr. (1978). Responses of cerebral arteries and arterioles to acute hypotension and hypertension. Am. J. Physiol. *234*, 371–383.

5. Shih, A.Y., Rühlmann, C., Blinder, P., Devor, A., Drew, P.J., Friedman, B., Knutsen, P.M., Lyden, P.D., Mateo, C., Mellander, L., et al. (2015). Robust and fragile aspects of cortical blood flow in relation to the underlying angioarchitecture. Microcirculation *22*, 204–218.

6. Devor, A., Tian, P., Nishimura, N., Teng, I.C., Hillman, E.M.C., Narayanan, S.N., Ulbert, I., Boas, D.A., Kleinfeld, D., and Dale, A.M. (2007). Suppressed neuronal activity and concurrent arteriolar vasoconstriction may explain negative blood oxygenation level-dependent signaling. J. Neurosci. *27*, 4452–4459.

7. Schaffer, C.B., Friedman, B., Nishimura, N., Schroeder, L.F., Tsai, P.S., Ebner, F.F., Lyden, P.D., and Kleinfeld, D. (2006). Two-photon imaging of cortical surface microvessels reveals a robust redistribution in blood flow after vascular occlusion. PLoS Biol. *4*, e22.

8. Mateo, C., Knutsen, P.M., Tsai, P.S., Shih, A.Y., and Kleinfeld, D. (2017). Entrainment of arteriole vasomotor fluctuations by neural activity is a basis of blood oxygen level dependent "resting state" connectivity. Neuron *96*, 936–948.e3.

9. Winder, A.T., Echagarruga, C., Zhang, Q., and Drew, P.J. (2017). Weak correlations between hemodynamic signals and ongoing neural activity during the resting state. Nat. Neurosci. *20*, 1761–1769.

10. Ma, Y., Shaik, M.A., Kozberg, M.G., Kim, S.H., Portes, J.P., Timerman, D., and Hillman, E.M.C. (2016). Resting-state hemodynamics are spatiotemporally coupled to synchronized and symmetric neural activity in excitatory neurons. Proc. Natl. Acad. Sci. USA *113*, 8463–8471.

11. Nunez-Elizalde, A.O., Krumin, M., Reddy, C.B., Montaldo, G., Urban, A., Harris, K.D., and Carandini, M. (2022). Neural correlates of blood flow measured by ultrasound. Neuron *110*, 1631–1640.e4.

12. Emerson, G.G., and Segal, S.S. (2000). Electrical coupling between endothelial cells and smooth muscle cells in hamster feed arteries: Role in vasomotor control. Circ. Res. 87, 474–479.

13. Segal, S.S., and Duling, B.R. (1989). Conduction of vasomotor responses in arterioles: A role for cell-to-cell coupling? Am. J. Physiol. 256, 838–845.

14. Segal, S.S., Damon, D.N., and Duling, B.R. (1989). Propagation of vasomotor responses coordinates arteriolar resistances. Am. J. Physiol. 256, H832–H837.

15. Ermentrout, G.B., and Kleinfeld, D. (2001). Traveling electrical waves in cortex: Insights from phase dynamics and speculation on a computational role. Neuron 29, 33–44.

16. Longden, T.A., Dabertrand, F., Koide, M., Gonzales, A.L., Tykocki, N.R., Brayden, J.E., Hill-Eubanks, D., and Nelson, M.T. (2017). Capillary K^+-sensing initiates retrograde hyperpolarization to increase local cerebral blood flow. Nat. Neurosci. 20, 717–726.

17. Filosa, J.A., Bonev, A.D., Straub, S.V., Meredith, A.L., Wilkerson, M.K., Aldrich, R.W., and Nelson, M.T. (2006). Local potassium signaling couples neuronal activity to vasodilation in the brain. Nat. Neurosci. 9, 1397–1403.

18. Thakore, P., Alvarado, M.G., Ali, S., Mughal, A., Pires, P.W., Yamasaki, E., Pritchard, H.A., Isakson, B.E., Tran, C.H.T., and Earley, S. (2021). Brain endothelial cell TRPA1 channels initiate neurovascular coupling. Elife 10, e63040.

19. Drew, P.J., Mateo, C., Turner, K.L., Yu, X., and Kleinfeld, D. (2020). Ultraslow oscillations in fMRI and resting state connectivity: Neuronal and vascular contributions and technical confounds. Neuron 107, 782–804.

20. Drew, P.J., Shih, A.Y., and Kleinfeld, D. (2011). Fluctuating and sensory-induced vasodynamics in rodent cortex extends arteriole capacity. Proc. Natl. Acad. Sci. USA 108, 8473–8478.

21. Blinder, P., Tsai, P.S., Kaufhold, J.P., Knutsen, P.M., Suhl, H., and Kleinfeld, D. (2013). The murine cortical angiome: An interconnected vascular network with noncolumnar patterns of blood flow. Nat. Neurosci. 16, 889–897.

22. Gould, I.G., Tsai, P., Kleinfeld, D., and Linninger, A. (2017). The capillary bed offers the largest hemodynamic resistance to the cortical blood supply. J. Cereb. Blood Flow Metab. 37, 52–68.

23. Schmid, F., Tsai, P.S., Kleinfeld, D., Jenny, P., and Weber, B. (2017). Depth dependant flow and pressure characteristics in cortical microvascular networks. PLoS Comput. Biol. 13, e1005392.

24. Tsai, A.G., and Intaglietta, M. (1993). Evidence of flowmotion induced changes in local tissue oxygenation. Int. J. Microcirc. Clin. Exp. 12, 75–88.

25. Goldman, D., and Popel, A.S. (2001). A computational study of the effect of vasomotion on oxygen transport from capillary networks. J. Theor. Biol. 209, 189–199.

26. Hapuarachchi, T., Park, C.S., and Payne, S. (2010). Quantification of the effects of vasomotion on mass transport to tissue from axisymmetric blood vessels. J. Theor. Biol. 264, 553–559.

27. Munting, L.P., Bonnar, O., Kozberg, M.G., Auger, C.A., Hirschler, L., Hou, S.S., Greenberg, S.M., Bacskai, B.J., and van Veluw, S.J. (2023). Spontaneous vasomotion propagates along pial arterioles in the awake mouse brain like stimulus-evoked vascular reactivity. J. Cereb. Blood Flow Metab. 43, 1752–1763.

28. Rungta, R.L., Chaigneau, E., Osmanski, B.F., and Charpak, S. (2018). Vascular compartmentalization of functional hyperemia from the synapse to the pia. Neuron 99, 362–375.e4.

29. Tian, P., Teng, I.C., May, L.D., Kurz, R., Lu, K., Scadeng, M., Hillman, E.M.C., De Crespigny, A.J., D'Arceuil, H.E., Mandeville, J.B., et al. (2010). Cortical depth-specific microvascular dilation underlies laminar differences in blood oxygenation level-dependent functional MRI signal. Proc. Natl. Acad. Sci. USA 107, 15246–15251.

30. Kedarasetti, R.T., Drew, P.J., and Costanzo, F. (2022). Arterial vasodilation drives convective fluid flow in the brain: a poroelastic model. Fluids Barriers CNS 19, e34.

31. van Veluw, S.J., Hou, S.S., Calvo-Rodriguez, M., Arbel-Ornath, M., Snyder, A.C., Frosch, M.P., Greenberg, S.M., and Bacskai, B.J. (2020). Vasomotion as a driving force for paravascular clearance in the awake mouse brain. Neuron 105, 549–561.e5.

32. Iliff, J.J., Wang, M., Zeppenfeld, D.M., Venkataraman, A., Plog, B.A., Liao, Y., Deane, R., and Nedergaard, M. (2013). Cerebral arterial pulsation drives paravascular CSF–interstitial fluid exchange in the murine brain. J. Neurosci. 33, 18190–18199.

33. Drew, P.J., Shih, A.Y., Driscoll, J.D., Knutsen, P.M., Blinder, P., Davalos, D., Akassoglou, K., Tsai, P.S., and Kleinfeld, D. (2010). Chronic optical access through a polished and reinforced thinned skull. Nat. Methods 7, 981–984.

34. Liu, R., Li, Z., Marvin, J.S., and Kleinfeld, D. (2019). Direct wavefront sensing enables functional imaging of infragranular axons and spines. Nat. Methods 16, 615–618.

35. Chen, B., Chakraborty, T., Daetwyler, S., Manton, J.D., Dean, K., and Fiolka, R. (2020). Extended depth of focus multiphoton microscopy via incoherent pulse splitting. Biomed. Opt Express 11, 3830–3842.

36. Nishimura, N., Schaffer, C.B., Friedman, B., Lyden, P.D., and Kleinfeld, D. (2007). Penetrating arterioles are a bottleneck in the perfusion of neocortex. Proc. Natl. Acad. Sci. USA 104, 365–370.

37. Hill, D.N., Curtis, J.C., Moore, J.D., and Kleinfeld, D. (2011). Primary motor cortex reports efferent control of vibrissa position on multiple time scales. Neuron 72, 344–356.

38. Chen, B.R., Bouchard, M.B., McCaslin, A.F.H., Burgess, S.A., and Hillman, E.M.C. (2011). High-speed vascular dynamics of the hemodynamic response. Neuroimage 54, 1021–1030.

39. Gao, Y.R., Greene, S.E., and Drew, P.J. (2015). Mechanical restriction of intracortical vessel dilation by brain tissue sculpts the hemodynamic response. Neuroimage 115, 162–176.

40. O'Herron, P.J., Hartmann, D.A., Xie, K., Kara, P., and Shih, A.Y. (2022). 3D optogenetic control of arteriole diameter in vivo. Elife 11, e72802.

41. Lin, J.Y., Knutsen, P.M., Muller, A., Kleinfeld, D., and Tsien, R.Y. (2013). ReaChR: A red-shifted variant of channelrhodopsin enables neuronal activation through the intact skull. Nat. Neurosci. 16, 1499–1508.

42. Cuttler, A.S., LeClair, R.J., Stohn, J.P., Wang, Q., Sorenson, C.M., Liaw, L., and Lindner, V. (2011). Characterization of Pdgfrb-Cre transgenic mice reveals reduction of ROSA26 reporter activity in remodeling arteries. Genesis 49, 673–680.

43. Guyton, A.C., and Hall, J.E. (2006). Textbook of Medical Physiology (Elsevier Saunders).

44. Gao, Y.-R., and Drew, P.J. (2014). Determination of vessel cross-sectional area by thresholding in radon space. J. Cereb. Blood Flow Metab. 34, 1180–1187.

45. Dong, H.W. (2008). The Allen Reference Atlas: A Digital Color Brain Atlas of the C57Bl/6J Male Mouse (John Wiley & Sons Inc.).

46. Hill, R.A., Tong, L., Yuan, P., Murikinati, S., Gupta, S., and Grutzendler, J. (2015). Regional blood fow in the normal and ischemic brain is controlled by arteriolar smooth muscle cell contractility and not by capillary pericytes. Neuron 87, 95–110.

47. Glück, C., Ferrari, K.D., Binini, N., Keller, A., Saab, A.S., Stobart, J.L., and Weber, B. (2021). Distinct signatures of calcium activity in brain mural cells. Elife 10, e70591.

48. Ohkura, M., Sasaki, T., Sadakari, J., Gengyo-Ando, K., Kagawa-Nagamura, Y., Kobayashi, C., Ikegaya, Y., and Nakai, J. (2012). Genetically encoded green fluorescent Ca^{2+} indicators with improved detectability for neuronal Ca^{2+} signals. PLoS One 7, e51286.

49. Hill, M.A., Zou, H., Potocnik, S.J., Meininger, G.A., and Davis, M.J. (2001). Invited review: Arteriolar smooth muscle mechanotransduction:

Ca²⁺ signaling pathways underlying myogenic reactivity. J. Appl. Physiol. *91*, 973–983.

50. Mohajerani, M.H., Chan, A.W., Mohsenvand, M., Ledue, J., Liu, R., McVea, D.A., Boyd, J.D., Wang, Y.T., Reimers, M., and Murphy, T.H. (2013). Spontaneous cortical activity alternates between motifs defined by regional axonal projections. Nat. Neurosci. *16*, 1426–1435.

51. Somiyo, A.P., and Somiyo, A.V. (1994). Signal transduction and regulation in smooth muscle. Nature *372*, 231–236.

52. Mann, M.E., and Park, J. (1994). Global-scale modes of surface temperature variability on interannual to centuries timescales. J. Geophys. Res. *99*, 25819–25833.

53. Shmuel, A., and Leopold, D.A. (2008). Neuronal correlates of spontaneous fluctuations in fMRI signals in monkey visual cortex: Implications for functional connectivity at rest. Hum. Brain Mapp. *29*, 751–761.

54. Schölvinck, M.L., Maier, A., Ye, F.Q., Duyn, J.H., and Leopold, D.A. (2010). Neural basis of global resting-state fMRI activity. Proc. Natl. Acad. Sci. USA *107*, 10238–10243.

55. Theis, L., Berens, P., Froudarakis, E., Reimer, J., Román Rosón, M., Baden, T., Euler, T., Tolias, A.S., and Bethge, M. (2016). Benchmarking spike rate inference in population calcium imaging. Neuron *90*, 471–482.

56. Charles, A.S., Cermak, N., Affan, R.O., Scott, B.B., Schiller, J., and Mishne, G. (2022). GraFT: Graph filtered temporal dictionary learning for functional neural imaging. IEEE Trans. Image Process. *31*, 3509–3524.

57. Aalkjaer, C., and Nilsson, H. (2005). Vasomotion: Cellular background for the oscillator and for the synchronization of smooth muscle cells. Br. J. Pharmacol. *144*, 605–616.

58. Hundley, W.G., Renaldo, G.J., Levasseur, J.E., and Kontos, H.A. (1988). Vasomotion in cerebral microcirculation of awake rabbits. Am. J. Physiol. *254*, 67–71.

59. Mayhew, J.E., Askew, S., Zheng, Y., Porrill, J., Westby, G.W., Redgrave, P., Rector, D.M., and Harper, R.M. (1996). Cerebral vasomotion: 0.1 Hz oscillation in reflectance imaging of neural activity. Neuroimage *4*, 183–193.

60. Pradhan, R.K., and Chakravarthy, V.S. (2011). Informational dynamics of vasomotion in microvascular networks: A review. Acta Physiol. *201*, 193–218.

61. Mitra, P.P., Ogawa, S., Hu, X., and Uğurbil, K. (1997). The nature of spatiotemporal changes in cerebral hemodynamics as manifested in functional magnetic resonance imaging. Magn. Reson. Med. *37*, 511–518.

62. Razavi, M., Eaton, B., Paradiso, S., Mina, M., Hudetz, A.G., and Bolinger, L. (2008). Source of low-frequency fluctuations in functional MRI signal. J. Magn. Reson. Imaging. *27*, 891–897.

63. Fox, M.D., and Raichle, M.E. (2007). Spontaneous fluctuations in brain activity observed with functional magnetic resonance imaging. Nat. Rev. Neurosci. *8*, 700–711.

64. Biswal, B., Yetkin, F.Z., Haughton, V.M., and Hyde, J.S. (1995). Functional connectivity in the motor cortex of resting human brain using echo-planar MRI. Magn. Reson. Med. *34*, 537–541.

65. Magnuson, M.E., Thompson, G.J., Pan, W.-J., and Keilholz, S.D. (2014). Effects of severing the corpus callosum on electrical and BOLD functional connectivity and spontaneous dynamic activity in the rat brain. Brain Connect. *4*, 15–29.

66. He, Y., Wang, M., Chen, X., Pohmann, R., Polimeni, J.R., Scheffler, K., Rosen, B.R., Kleinfeld, D., and Yu, X. (2018). Ultra-slow single-vessel BOLD and CBV-based fMRI spatiotemporal dynamics and their correlation with neuronal intracellular calcium signals. Neuron *97*, 925–939.e5.

67. Rungta, R.L., Zuend, M., Aydin, A.-K., Martineau, É., Boido, D., Weber, B., and Charpak, S. (2021). Diversity of neurovascular coupling dynamics along vascular arbors in layer II/III somatosensory cortex. Commun. Biol. *4*, e855.

68. Stefanovic, B., Hutchinson, E., Yakovleva, V., Schram, V., Russell, J.T., Belluscio, L., Koretsky, A.P., and Silva, A.C. (2008). Functional reactivity of cerebral capillaries. J. Cereb. Blood Flow Metab. *28*, 961–972.

69. Kleinfeld, D., Mitra, P.P., Helmchen, F., and Denk, W. (1998). Fluctuations and stimulus-induced changes in blood flow observed in individual capillaries in layers 2 through 4 of rat neocortex. Proc. Natl. Acad. Sci. USA *95*, 15741–15746.

70. Shih, A.Y., Blinder, P., Tsai, P.S., Friedman, B., Stanley, G., Lyden, P.D., and Kleinfeld, D. (2013). The smallest stroke: Occlusion of one penetrating vessel leads to infarction and a cognitive deficit. Nat. Neurosci. *16*, 55–63.

71. Pagani, G.A., and Aiello, M. (2013). The power grid as a complex network: A survey. Phys. Stat. Mech. Appl. *392*, 2688–2700.

72. Boorman, L.W., Harris, S.S., Shabir, O., Lee, L., Eyre, B., Howarth, C., and Berwick, J. (2023). Bidirectional alterations in brain temperature profoundly modulate spatiotemporal neurovascular responses in-vivo. Commun. Biol. *6*, e185.

73. Jack, J.J.B., Noble, D., and Tsien, R.W. (1974). Electric Current Flow in Excitable Cells (Clarendon Press).

74. Aldea, R., Weller, R.O., Wilcock, D.M., Carare, R.O., and Richardson, G. (2019). Cerebrovascular smooth muscle cells as the drivers of intramural periarterial drainage of the brain. Front. Aging Neurosci. *11*, 1–17.

75. Hladky, S.B., and Barrand, M.A. (2022). The glymphatic hypothesis: The theory and the evidence. Fluids Barriers CNS *19*, 9.

76. Holstein-Rønsbo, S., Gan, Y., Giannetto, M.J., Rasmussen, M.K., Sigurdsson, B., Beinlich, F.R.M., Rose, L., Untiet, V., Hablitz, L.M., Kelley, D.H., and Nedergaard, M. (2023). Glymphatic influx and clearance are accelerated by neurovascular coupling. Nat. Neurosci. *26*, 1042–1053.

77. Jiang-Xie, L.-F., Drieu, A., Bhasiin, K., Quintero, D., Smirnov, I., and Kipnis, J. (2024). Neuronal dynamics direct cerebrospinal fluid perfusion and brain clearance. Nature *627*, 157–164.

78. Miao, A., Luo, T., Hsieh, B., Edge, C.J., Gridley, M., Wong, R.T.C., Constadinou, T.G., Wisden, W., and Franks, N.P. (2024). Brain clearance is reduced during sleep and anesthesia. Nat. Neurosci. Published online May 13, 2014. https://doi.org/10.1038/s41593-024-01638-y.

79. Xie, L., Kang, H., Xu, Q., Chen, M.J., Liao, Y., Thiyagarajan, M., O'Donnell, J., Christensen, D.J., Nicholson, C., Iliff, J.J., et al. (2013). Sleep drives metabolite clearance from the adult brain. Science *342*, 373–377.

80. Sangalli, L., and Boggero, I.A. (2023). The impact of sleep components, quality and patterns on glymphatic system functioning in healthy adults: A systematic review. Sleep Med. *101*, 322–349.

81. Christensen, J., Yamakawa, G.R., Shultz, S.R., and Mychasiuk, R. (2021). Is the glymphatic system the missing link between sleep impairments and neurological disorders? Examining the implications and uncertainties. Prog. Neurobiol. *198*, e101917.

82. Fultz, N.E., Bonmassar, G., Setsompop, K., Stickgold, R.A., Rosen, B.R., Polimeni, J.R., and Lewis, L.D. (2019). Coupled electrophysiological, hemodynamic, and cerebrospinal fluid oscillations in human sleep. Science *366*, 628–631.

83. Kedarasetti, R.T., Turner, K.L., Echagarruga, C., Gluckman, B.J., Drew, P.J., and Costanzo, F. (2020). Functional hyperemia drives fluid exchange in the paravascular space. Fluids Barriers CNS *17*, e52.

84. Tønnesen, J., Inavalli, V.K., and Nägerl, U.V. (2018). Super-resolution imaging of the extracellular epace in living brain tissue. Cell *172*, 1108–1121.e15.

85. Albargothy, N.J., Johnston, D.A., MacGregor-Sharp, M., Weller, R.O., Verma, A., Hawkes, C.A., and Carare, R.O. (2018). Convective influx/glymphatic system: tracers injected into the CSF enter and leave the brain along separate periarterial basement membrane pathways. Acta Neuropathol. *136*, 139–152.

86. Fox, M.D., Snyder, A.Z., Vincent, J.L., Corbetta, M., Van Essen, D.C., and Raichle, M.E. (2005). The human brain is intrinsically organized into dynamic, anticorrelated functional networks. Proc. Natl. Acad. Sci. USA *102*, 9673–9678.

87. Glasser, M.F., Coalson, T.S., Robinson, E.C., Hacker, C.D., Harwell, J., Yacoub, E., Ugurbil, K., Andersson, J., Beckmann, C.F., Jenkinson, M., et al. (2016). A multi-modal parcellation of human cerebral cortex. Nature *536*, 171–178.

88. Lake, E.M.R., Ge, X., Shen, X., Herman, P., Hyder, F., Cardin, J.A., Higley, M.J., Scheinost, D., Papademetris, X., Crair, M.C., and Constable, R.T. (2020). Simultaneous cortex-wide fluorescence Ca^{2+} imaging and whole-brain fMRI. Nat. Methods *17*, 1262–1271.

89. Drew, P.J., Duyn, J.H., Golanov, E., and Kleinfeld, D. (2008). Finding coherence in spontaneous oscillations. Nat. Neurosci. *11*, 991–993.

90. Das, A., Murphy, K., and Drew, P.J. (2021). Rude mechanicals in brain haemodynamics: non-neural actors that influence blood flow. Philos. Trans. R. Soc. Lond. B Biol. Sci. *376*, 20190635.

91. Koenigsberger, M., Sauser, R., Bény, J.-L., and Meister, J.-J. (2006). Effects of arterial wall stress on vasomotion. Biophys. J. *91*, 1663–1674.

92. Stergiopulos, N., Porret, C.-A., De Brouwer, S., and Meister, J.-J. (1998). Arterial vasomotion: Effect of flow and evidence of nonlinear dynamics. Am. J. Physiol. *274*, 1858–1864.

93. Yao, P., Liu, R., Broggini, T., Thunemann, M., and Kleinfeld, D. (2023). Construction and use of an adaptive optics two-photon microscope with direct wavefront sensing. Nat. Protoc. *18*, 3732–3766.

94. Ma, Y., Shaik, M.A., Kim, S.H., Kozberg, M.G., Thibodeaux, D.N., Zhao, H.T., Yu, H., and Hillman, E.M.C. (2016). Wide-field optical mapping of neural activity and brain haemodynamics: Considerations and novel approaches. Philos. Trans. R. Soc. Lond. B Biol. Sci. *371*, 20150360.

95. Svoboda, K., Denk, W., Kleinfeld, D., and Tank, D.W. (1997). *In vivo* dendritic calcium dynamics in neocortical pyramidal neurons. Nature *385*, 161–165.

96. Prendergasr, B.J., Onishi, K.G., and Zucker, I. (2014). Female mice liberated for inclusion in neuroscience and biomedical research. Neurosci. Biobehav. Rev. *40*, 1–5.

97. Levy, D.R., Hunter, N., Lin, S., Robinson, E.M., Gillis, W., Conlin, E.B., Anyoha, R., Shansky, R.M., and Datta, S.R. (2023). Mouse spontaneous behavior reflects individual variation rather than estrous state. Curr. Biol. *33*, 1358–1364.e4.

98. Kornfield, T.E., and Newman, E.A. (2015). Measurement of retinal blood flow using fluorescently labeled red blood cells. eNeuro *2*, ENEURO.0005-15.2015. https://doi.org/10.1523/ENEURO.0005-1515.2015.

99. Shaked, I., Hanna, R.N., Shaked, H., Chodaczek, G., Nowyhed, H.N., Tweet, G., Tacke, R., Basat, A.B., Mikulski, Z., Togher, S., et al. (2015). Transcription factor Nr4a1 couples sympathetic and inflammatory cues in CNS-recruited macrophages to limit neuroinflammation. Nat. Immunol. *16*, 1228–1234.

100. Ji, X., Ferreira, T., Friedman, B., Liu, R., Liechty, H., Bas, E., Chandrashekar, J., and Kleinfeld, D. (2021). The brain microvasculature has a common topology with local differences in geometry that match metabolic load. Neuron *109*, 1168–1187.e13.

101. Holtmaat, A., Bonhoeffer, T., Chow, D.K., Chuckowree, J., De Paola, V., Hofer, S.B., Hübener, M., Keck, T., Knott, G., Lee, W.C.A., et al. (2009). Long-term, high-resolution imaging in the mouse neocortex through a chronic cranial window. Nat. Protoc. *4*, 1128–1144.

102. Barrett, M.J.P., Ferrari, K.D., Stobart, J.L., Holub, M., and Weber, B. (2018). CHIPS: an extensible toolbox for cellular and hemodynamic two-photon image analysis. Neuroinformatics *16*, 145–147.

103. Kleinfeld, D., and Mitra, P.P. (2011). Applications of spectral methods in functional brain imaging. In Imaging: A Laboratory Manual, R. Yuste, ed. (Cold Spring Harbor Laboratory Press), pp. 12.11–12.17.

104. Zar, J.H. (2010). Biostatistical Analysis (Pearson Education).

105. Tsai, P.S., Mateo, C., Field, J.J., Schaffer, C.B., Anderson, M.E., and Kleinfeld, D. (2015). Ultra–large field-of-view two-photon laser scanning microscopy. Opt Express *23*, 13833–13847.

106. Edelstein, A.D., Tsuchida, M.A., Amodaj, N., Pinkard, H., Vale, R.D., and Stuurman, N. (2014). Advanced methods of microscope control using μManager software. J. Biol. Methods *1*, e10.

107. Percival, D.B., and Walden, A.T. (1993). Spectral Analysis for Physical Applications: Multitaper and Conventional Univariate Techniques (Cambridge University Press).

108. Prechtl, J.C., Cohen, L.B., Pesaran, B., Mitra, P.P., and Kleinfeld, D. (1997). Visual stimuli induce waves of electrical activity in turtle cortex. Proc. Natl. Acad. Sci. USA *94*, 7621–7626.

109. Jarvis, M.R., and Mitra, P.P. (2001). Sampling properties of the spectrum and coherency of sequences of action potentials. Neural Comput. *13*, 717–749.

110. Kleinfeld, D., Sachdev, R.N.S., Merchant, L.M., Jarvis, M.R., and Ebner, F.F. (2002). Adaptive filtering of vibrissa input in motor cortex of rat. Neuron *34*, 1021–1034.

111. Aljadeff, J., Lansdell, B.J., Fairhall, A.L., and Kleinfeld, D. (2016). Analysis of neuronal spike trains, deconstructed. Neuron *91*, 221–259.

STAR★METHODS

KEY RESOURCES TABLE

REAGENT or RESOURCE	SOURCE	IDENTIFIER
Chemicals, peptides, and recombinant proteins		
Isoflurane	Henry Schein	Cat # 1182097
Buprenorphine Hydrochloride, injection	Par Pharmaceutical	Cat # 110483373347
Cyanoacrylate glue, Loctite 401	MacMaster-Carr	Loctite 401
Cy5.5 – dextran (2 MDa)	Self-synthesized	Liu et al., 2019
Experimental models: Organisms/strains		
Mouse: C57Bl6/J	Jackson Laboratories	# 000664
Mouse: B6.Cg-Tg(Acta2-GCaMP8.1/mVermilion) B34-4Mik/J	Jackson Laboratories	# 032887
Mouse: Tg(Thy1-jRGECO1a)GP8.20Dkim/J	Jackson Laboratories	# 030525
Mouse: Tg(PDGFRβ-cre)35Vli	Volkhard Lindner	Cuttler et al.[42]
Mouse: B6.Cg-Gt(ROSA)26Sortm2.2Ksvo/J	Jackson Laboratories	# 026294
Software and algorithms		
MATLAB	MathWorks	N/A
ScanImage	MBF Bioscience	N/A
Chronux	Chronux.org	N/A
MicroManager 2	Micromanager.org	N/A
Photoshop 2022	Adobe Inc.	N/A
Illustrator 2022	Adobe Inc.	N/A
Analysis software	GitHub	https://doi.org/10.5281/zenodo.11041234
Other		
Processed data	DANDI	https://dandiarchive.org/dandiset/000970
PowerLab	AD Instruments	Cat # 16/35
Prime95B	Photometrics	Cat # Prime95B
Two-photon microscope with adaptive optics	Thorlabs and others	Liu et al.[34,93]
SteREO Discovery.V8	Zeiss	N/A

RESOURCE AVAILABILITY

Lead contact
Further information and requests for resources and reagents should be directed to and will be fulfilled by Prof. David Kleinfeld (dk@physics.ucsd.edu).

Materials availability
This study did not generate new unique reagents.

Data and code availability
- All processed data is deposited at DANDI and is publicly available. The URL is listed in the key resources table. Microscopy data used for this study will be shared by the lead contact upon request.
- All original code has been deposited at Zenodo and is publicly available as of the date of publication. The DOI is listed in the key resources table.
- Any additional information required to reanalyze the data reported in this paper is available from the lead contact upon request.

EXPERIMENTAL MODEL AND STUDY PARTICIPANT DETAILS

Experimental subjects
All animal procedures were approved by the Institutional Animal Care and Use Committee at the University of California, San Diego (UCSD) and were performed under the guidance of the UC San Diego Center for Animal Resources and Education.

We used three strains of mice.

(1) One was a double transgenic B6.Cg-Tg(Acta2-GCaMP8.1/mVermilion)B34-4Mik/J (JAX no. 032887) line expressing GCaMP8.1 in smooth muscle crossed with transgenic Tg(Thy1-jRGECO1a)GP8.20Dkim/J (JAX no. 030525) neuronal jRGE-CO1a expressing mice both with congeneric background. The resulting double-positive animals (24 mice; 16 female and 8 male), with ages between P48 and P366, were used in all widefield imaging experiments.[94] The single positive smooth muscle GCaMP8.1 animals (3 female mice) with ages between P157 and P231 were used for a set of calibration runs with two-photon microscopy.

(2) The second was C57Bl6/J wild type mice (JAX no. 000664) (16 male mice) with ages between P73 and P192. These were used exclusively for two-photon imaging experiments.[69,95]

(3) The third strain was Tg(PDGFRβ-cre)35Vli generated by Volkhard Lindner[42] (MGI:5291826) expressing cre in pericytes and smooth muscle cells crossed with B6.Cg-Gt(ROSA)26Sortm2.2Ksvo/J generated by Karel Svoboda (Jax: Stock No: 026294) containing a CAG-LSL-ReaChR-mCit gene cassette in the Rosa26 locus. The double-positive animals had been backcrossed to the C57Bl6 background for at least 6 generations. These animals (3 mice; 2 females and 1 male), with ages between P180 and P251, were used exclusively for two-photon optogenetic experiments.

Prior to surgery, all mice were housed one to five per cage with a 07:00 to 19:00 light-dark cycle. Variability across behavioral and physiological traits are not significantly greater in female rodents, including across the estrous cycle, than male rodents.[96,97]

METHOD DETAILS

Common surgical procedures

Mice were anesthetized with 4% (v/v) isoflurane in oxygen for induction and 1%–3% (v/v) for maintenance, from a precision vaporizer. Reflexes and breathing were visually monitored through the entire surgical procedure to ensure a deep plane of anesthesia. Body temperature was maintained at 37°C with a heating pad with feedback regulation (FHC, no. 40-90-8D). The animal was placed in a stereotaxic frame and the skull over cortex was thinned with a 250-μm drill burr coupled to a low vibration drill (Osada, EXL-M40) to form a thinned skull window.[33] The thinned bone was dried and covered with cyanoacrylate glue (Loctite no. 401) and a number 0 glass coverslip. Areas of different sizes were thinned for different preparations, are detailed below. A titanium implant was glued onto the cerebellar part of the skull for head-fixation. All exposed bone and the implant were covered with cyanoacrylate glue and dental cement (Grip Cement, Dentsply no. 675571) to increase stability. Buprenorphine hydrochloride (Buprenex, Reckitt Benckiser Pharmaceuticals) was provided subcutaneously for analgesia (0.1 mg/kg body weight) as the animal recovered from surgery.

Common post-surgical preparation

After a minimum of 48-h post surgery, mice were handled and trained to head fixation in sessions of 20–180 min for two days and additionally three days of 120-to-180-min sessions under the microscope, with the imaging light emitting diodes (LED) operating. Equivalent training sessions were used before two-photon imaging experiments.

Simultaneous diameter and flux measurements

These made use of wild-type mice. We imaged pial artery diameters and sparsely labeled red blood cell (RBC) flux in pial vessels across the mouse vibrissa primary sensory (vS1) cortex through a thinned skull preparation[33] with a 3 mm diameter window. These measurements made use of adaptive optics two-photon microscopy[34] with the addition of a resonant scanner (CRS8K, Cambridge Technology) and a layered beam splitter mask[35] (Figure 1A) to extend the depth of the focus. We injected 50 μL of 2 MDa CY5.5-dextran retro-orbitally into the bloodstream for visualizing the vessel lumen.[34] A small fraction of RBCs from littermate mice were isolated from the blood, labeled with dye,[98] CellTrace CFSE (ThermoFisher) that bound to their membrane, and injected into the mouse.[99] After identifying a pial artery, we parked the y-direction galvo and scanned x-direction resonant scanner along the radial direction of the vessel at about 16 kHz with a sampling pixel size of 0.5 μm. A motorized rotation stage (RSM40B-T4A, Zaber) was used to align the radial direction of the measured vessel to the scanning direction of the resonant scanner. To avoid damage to the vessel, each imaging section lasted for only 2 min and five imaging sections were acquired for each selected vessel. Incident imaging power ranged from 28 to 83 mW in resting state trials, 59 to 102 mW for 0.1 Hz air puff stimulation trials, and 47 to 59 mW in ReaChR activation trials. Each trial's power was kept at the minimum required to reliably image RBCs, given differences in RBC labeling between trials and differences in thin-skull thickness between locations.

Two channels of line scans were acquired: one for measuring vessel diameter and the other for flux of the labeled RBCs. For both channels, every 312 lines of the scan were concatenated into a frame, resulting in an effective frame rate of 50.2 Hz (ScanImage, Vidrio Technologies). For the diameter channel, each frame was smoothed by a two-dimensional 3-by-3 medial filter, and the average intensity profile over 1,898,400 lines was used to estimate the global signal-to-noise ratio (SNR). The position of the vessel in each frame was then estimated by the combination of Otsu thresholding and the estimated global SNR, followed by removing small connected components and morphological close operations.[100] The resulting vessel mask was used for both diameter and flux

measurements. For vessel diameter, the full width at half maximum (FWHM) of the intensity profile along each scanned line is estimated as the diameter of the vessel. Specifically, we defined each profile's maximum intensity as the median value more than three standard deviations above the frame's average background intensity. The half-maximum intensity was then midway between this maximum and the frame's average background. Linear interpolation was used to find the profile's two half-maximum crossing locations, whose separation distance was the FWHM. The diameter was measured with 20-ms resolution that was computed as the median of the 316 estimations in each frame. The outliers in the diameter trace were detected as estimates three standard deviations away from the mean in a 1-s moving window and were replaced by a linear interpolation of the deleted value.

For flux measurement, as RBCs were sparsely labeled, we assumed that 0.9 of the pixels inside the vessel mask were background and used their intensities to estimate the SNR level. For each frame, we computed the RBC mask based on the estimated SNR and further intersected this mask with the vessel mask to remove false positive detections outside the vessels. Connected components smaller than 10 pixels in the RBC mask were removed. The resulting RBC masks were concatenated into a single binary image for RBC detection. Each connected component was defined as a cell. The centroids of these connected components along the time axis were used to define the time when the cell passes the scanning position, while the standard deviation of the connected component intensity along the temporal axis is proportional to the passing time of an RBC if we neglect the potential rotation of the RBC within the period the cell passes the beam. The event of an RBC passing the scanning position can be modeled as a Poisson process. We computed the maximum likelihood estimate of the mean of the Poisson process as the number of RBCs detected every 20 ms.

To analyze the relationship between diameter and flux near the vasomotion frequency, the diameter and flux time series were further smoothed by a moving medial filter of window size 2-s. The smoothed diameter traces were used to compute the phase of the vasomotion. After subtracting the average vessel diameter of the imaging session, we computed the phase of the diameter using a modified Hilbert transform.[37] Peaks and troughs were detected from the smoothed diameter traces and a linear phase evolution was assumed between each pair of peaks and troughs. For each vessel segment, traces from five imaging sections were combined to compute the two-dimensional histograms.

For SMC activation experiments in PDGFRβ-cre crossed with ReaChR mice, the vessel wall mCitrine background was removed from RBC channel images by subtracting the median profile intensity over 20 ms from each frame. RBC detection was then restricted to the inner $\frac{3}{4}$ of the vessel to ensure no false RBC detections due to the fluorescent signal overlap from the vessel wall. The initial 0.2-decrease in diameter, and associated change in flux, were then used to quantify the flux-diameter relationship.

Penetrating vessel diameter measurements
These made use of awake, wild type mice with a 3.5 or 4-mm diameter chronic cranial window over vS1.[101] Mice were injected with 50 μL of 2 MDa CY5.5-dextran retroorbitaly to visualize the vessel lumen. We used the adaptive-optics two-photon microscope with resonant scanning[34] in addition to an objective piezo stage (nPFocus400, Motion Solution) for imaging at multiple depths. Penetrating vessels were scanned at two depths sequentially, up to 380 μm apart, at a 7.25 Hz volume frame rate and pixel size of 0.33 μm. Pial vessels were continuously imaged, and arterioles were identified by the presence of vasomotion. These arterioles were tracked, and the locations of PAs were noted. Each PA was scanned at two depths, for 10-min imaging sessions, up to 15 sessions per day per animal.

Penetrating vessel diameter extraction
Images at each depth were smoothed by a two-dimensional 5-by-5 medial filter for further analysis. To extract diameter, we used the previously developed Threshold in Radon Space (TiRS) method,[44] and adapted code from the TiRS implementation in the CHIPS toolbox.[102] The TiRS method was used because it is more robust to noise and changes in vessel shape than undirectional FWHM calculations.[44] First, each time point's image was radon transformed, normalized, and thresholded in radon space. This binary image in radon space was then inverse radon transformed, normalized, and thresholded again, generating a vessel cross section binary image. From this, we calculated the cross section's effective diameter as $D_{eff}(t) = \sqrt{4 * Area/\pi}$. We used thresholds of 0.4 and 0.2 for the radon space and inverse radon images respectively, and for some vessels adjusted the thresholds to values between 0.3 to 0.5 and 0.1 to 0.3. Frames with dD_{eff}/dt greater than 11 μm/s were detected and D_{eff} was replaced by a linear interpolation of D_{eff} from the surrounding frames. Longer duration artifacts were either manually replaced by the D_{eff} interpolation, or their time series were truncated to exclude the artifact.

Penetrating vessel spectral analysis
For penetrating vessel power spectra and phase calculations, we linearly interpolated the deep and shallow diameter time series to give each an effective sampling rate of 14.5 Hz. From here the multitaper method with half-bandwidth of 0.02 Hz and 23 tapers was used to calculate power spectra of each depth's diameter time series and the complex coherence between depths.[103] The vasomotor frequency was chosen as the frequency that maximized the shallow segment's power density within a user-defined window of approximately 0.02–0.2 Hz. Phase was calculated as the angle of the complex coherence at every frequency, with 95% CI found using the leave-one-taper out jackknife method in Chronux. For f vs. k plots and direction calculations, the phase gradient k was calculated as $\phi_{fv}/\sqrt{dz^2+dx^2}$, where ϕ_{fv} is the phase at the vasomotor frequency, dz is the vertical separation between vessel cross sections, and dx is the horizontal separation between cross sections. Vessels that didn't exhibit significant coherence between shallow and deep segments were excluded for f vs. k plots and direction calculations (6 of 146 vessels were excluded by this criteria).

CellPress

Travel direction spatial correlation calculation

We investigated the travel direction of PA vasomotion, calculating the travel direction correlation between PA pairs, followed by a binomial test on the average correlation at various distances. To calculate spatial correlation, for each vessel i we calculated the Euclidean distance to each other vessel j and $\sigma_i\sigma_j = \text{sign}(\boldsymbol{k}_i)*\text{sign}(\boldsymbol{k}_j)$. Because sign($\boldsymbol{k}$) (+1 or −1) is determined by the direction of the observed PA traveling wave (entering or exiting cortex), $\sigma_i\sigma_j = +1$ if two waves travel in the same direction, and $\sigma_i\sigma_j = −1$ if they travel in opposite directions. The $\sigma_i\sigma_j$ were calculated for every possible vessel pair, without repeats, within each imaging session i.e., N choose 2 pairs where N is the number of arterioles in the imaging session. The $\sigma_i\sigma_j$ values from all imaging sessions were concatenated and average spatial correlations, $<\sigma_i\sigma_j>$, were calculated as the average of all $\sigma_i\sigma_j$ having distance within a given distance bin. These $<\sigma_i\sigma_j>$ were plotted as black dots in Figure S5, with each distance bin containing 10 percent of all vessel pairs. Each average correlation is positive if there were more pairs traveling in the same direction and vice versa.

As measured across animals and trials, the probability of a wave exiting cortex is $p_{exit} = 85/140$ and the probability of a wave entering cortex is $p_{enter} = 1 − p_{exit} = 55/140$ (Figure 2F). It follows that $P(\sigma_i\sigma_j = +1) = p_{enter}^2 + p_{exit}^2$ which we define as p, and $P(\sigma_i\sigma_j = −1) = 2p_{enter}p_{exit}$ which we define as q. For a given number of PA pairs within a distance bin, N_{inbin}, the probability of measuring N_+ pairs with $\sigma_i\sigma_j = +1$ is given by the following binomial probability:

$$P(N_+) = \frac{N_{inbin}!}{N_+!(N_{inbin} - N_+)!}p^{N_+}q^{N_{inbin} - N_+}$$

We found critical N_+ values, $N_{+,0.025}$ and $N_{+,0.975}$, for which the cumulative probabilities $P(N_+ \leq N_{+,0.025}) = 0.025$ and $P(N_+ \leq N_{+,0.975}) = 0.975$ using the normal approximation to the binomial distribution.[104] The 95% confidence interval of $<\sigma_i\sigma_j>$ was then calculated as:

$$\left[\frac{N_{+,0.025} - (N_{inbin} - N_{+,0.025})}{N_{inbin}}, \frac{N_{+,0.975} - (N_{inbin} - N_{+,0.975})}{N_{inbin}}\right].$$

Simultaneous AO-2P measurements of smooth muscle calcium and arteriole diameter

After thin skull preparation, 50 μL of 2 MDa CY5.5-dextran was injected retroorbitaly to visualize the vessel lumen. Cy5.5 and the smooth muscle expressed GCaMP8.1 intensity fluctuations were measured simultaneously with multiphoton imaging. The Chameleon Discovery femtosecond laser source was tuned to 930 nm for excitation of both fluorophores. Frame scanning was performed over multiple vascular segments with a resonance scanner scan frequency of approximately 16 kHz and trial duration of 10 min. For each channel, images were background subtracted and every 3 frames were averaged together, resulting in a range of frame rates of 10.01–19.43 Hz after averaging. Lumen and GCaMP8.1 masks were created by averaging the first 100 s of Cy5.5 and GCaMP8.1 frames respectively, thresholding the images, and manually removing all non-artery areas.

To study SMC Ca^{2+} and dilation dynamics, we extracted GCaMP8.1 fluorescence, reported as $\Delta F(x,t)/\langle F(x)\rangle_t$, and diameter, $D(x,t)$, at corresponding locations along each vessel imaged (Figure 3C). First, the GCaMP8.1 mask was skeletonized and divided into segments according to the procedure used for widefield mask and vessel graph creation. Following this, $\Delta F(x,t)/\langle F(x)\rangle_t$ was calculated, where $F(x,t)$ was the mean intensity of pixels within each segment at each time point. We then extracted $D(x,t)$ from the Cy5.5 channel images at each GCaMP8.1 segment location. First the lumen mask was skeletonized, and diameter was estimated using MATLAB's "bwskel" and "bwdist" functions. Then, a set of 10 cross lines were calculated at each GCaMP8.1 segment location. These cross-lines were perpendicular to the lumen mask skeleton, with length as a constant multiple of the local lumen mask diameter; cross lines of 1.5 - to 2.5-times the vessel diameter were used. An example of these cross lines is plotted in Figure 3C.

Each Cy5.5 frame was median filtered using MATLAB's "medfilt2" within 9-pixel areas. Pixels comprising each line were found using the Bresenham line algorithm. Then each cross-line's intensity profile was found from these pixels and averaged across the 10 crosslines at each location. The resulting average profile was median filtered using MATLAB's "medfilt1" with filter order 6 and interpolated to enable sub-pixel diameter estimation. We then calculated $D(x,t)$ as the profile's full-width-(H')-max value (FWHM), where H'-max = baseline + (max(profile) − baseline)*H'. Here H' was 0.3 (instead of 0.5 for full-width-half-max) to avoid outliers caused by sporadically passing micrometer-sized particles. Finally, locations with poor $D(t)$ estimation due to underlying vein fluorescence were manually excluded. An example vessel's $\langle D(x,t)\rangle_x$ is plotted in Figure 3C (black).

Before calculating the cross correlation between GCaMP8.1 and diameter, movement time periods were classified and excluded to focus on resting-state dynamics and avoid any possible bias due to the vessel moving dramatically within the FOV. First, the mean Cy5.5 image was 2D cross-correlated with itself using MATLAB's "fft2" and "ifft2" functions, and the location of maximum correlation was recorded. Next, each frame was 2D cross-correlated with the mean image, and location of each frame's maximum correlation was recorded. Each frame's shift was calculated as the distance between these maxima. Time periods with frameshift exceeding 2σ of the trial's frameshift were found, and the 10 s before and after these were excluded. Remaining time periods shorter than 100 s were also excluded.

The normalized cross correlation between GCaMP8.1 $\Delta F/F$ and diameter were calculated at each vessel segment, for each time-period using MATLAB's "xcorr" function. For each vessel, the median peak magnitude correlation and lag at peak magnitude correlation across locations and time periods was plotted in Figure 3D. These were plotted against each vessel's average diameter across all locations and time. All correlation vs. lag curves were linearly interpolated to a common set of lags, and averaged over

vessels, locations, and time periods to obtain the average curve in the inset to Figure 3D. Error bars are the jackknife SE using leave-one location and time period-out estimates.

Simultaneous widefield measurements of pial arterioles and cortical neurons

These made use of crossed mice with GCaMP8.1 in arteriole smooth muscles and jRGECO1a in excitatory neurons. We used an extended thinned skull window that spanned an approximately 10 mm by 10 mm region of skull over the cortical mantle.[8,105] One photon frame-based imaging utilized a Zeiss SteREO Discovery V8 equipped with a custom filter cube (KSC 295-CUSTOM, Kramer Scientific, LLC) carrying a reflective mirror and ZET488/561m emission filter (Chroma). Dual color imaging was achieved using inter-laced activation of two LEDs at approximately 10 Hz (470 nm center wavelength; ThorLabs no. M470L3; Chroma ET470/40x and 565 nm ThorLabs no. SOLIS-4C; Semrock no. FF01-560/14–25) coupled to a liquid lightguide. Image acquisition was performed with a Prime95B 1200 by 1200 sCMOS camera (Teledyne Photometrics) running MicroManager 2 software.[106]

Mask creation and dF/F calculation from widefield data

To create each trial's pial arteriole mask, we took the standard deviation over time of the trial's first 1250 diffusion filtered GCaMP8.1 fluorescence images. The result was normalized and contrast-enhanced using MATLAB's "adapthisteq" function. Adobe Photoshop was used to sharpen, threshold, and manually connect pial arteriole segments that fell below the threshold. The thin-skull window edge was then manually defined and saved as the "rim" mask. The neural mask was defined as the rim mask area, excluding the pial arteriole mask, i.e., the relative complement of the pial mask in the rim.

The pial arteriole mask was used to define a vessel graph using procedures developed for reconstruction of the 3-dimensional microvascular connectome.[100] Briefly, the two-dimensional mask was skeletonized and diameter was estimated using MATLAB's "bwskel" and "bwdist" respectively. Skeleton pixels, which define the vessel centerline, were classified as either an endpoint, a link that connects two neighbors, or a node that connects three or more neighbors. Skeleton pixels were downsampled and dilated by the vessel diameter to define skeleton segments (Figure S6C). We then calculated the raw fluorescence signal $F(x,t)$ as the median intensity of pixels within each skeleton segment at each time point. Finally, $\Delta F(x,t)/\langle F(x,t)\rangle$ was calculated and stored for subsequent analyses, where $\Delta F(x,t) = F(x,t) - \langle F(x,t)\rangle$ and $\langle F(x,t)\rangle$ denotes the time-averaged intensity at each location x.

Phase-gradient calculation from widefield data

The vessel graph was further processed to isolate vessel segments longer than 0.75 mm for phase gradient analysis. Skeleton links shorter than 0.4 mm with only one connected node were removed from the graph, and remaining links were joined at nodes connected to two links. Distance was calculated as the cumulated sum of Euclidean distance between adjacent skeleton segment mid-points. The peak vasomotor frequency was calculated using the multitaper method with half-bandwidth 0.01 Hz for 500 s trials, 0.02 Hz for 250 s trials, and 9 tapers. Within each link, power spectra for each skeleton segment's $\Delta F(x,t)/\langle F(x)\rangle_t$ trace were averaged to find the frequency that maximized power within the approximately 0.02 Hz–0.2 Hz frequency band. This band was chosen manually for each trial to avoid selection of low frequency, i.e., $\sim$ 0.02 Hz–0.05 Hz, shoulders.

The phase of each skeleton segment was calculated with respect to the vessel's initial skeleton segment $\Delta F(x,t)/F(x)\rangle_t$ signal as the angle of the coherence at the vasomotor peak frequency. Here to calculate the coherence we used the multitaper method with a half-bandwidth of 0.03 Hz for 500 s trials, 0.06 Hz for 250 s trials, and 29 tapers. The phase gradient was calculated as the slope of the phase versus distance linear regression. To exclude vessel segments that exhibited poor correlation between phase and distance, a two tailed t test was performed on each vessel's correlation coefficient with H_0: $r = 0$ and $t = r/s_r$. Here s_r is the correlation coefficient's standard error, defined as $s_r = \sqrt{\frac{1-r^2}{n-2}}$ where n is the number of points in the regression.[104] For various significance levels α, we calculated $t_{critical}$ values, and excluded vessels with $|t| < t_{critical}$.

To study the neural signal near individual vessels, we defined an envelope surrounding each vessel segment (Figure S6C). This envelope starts 17 μm and extends to 70 μm from the edge of the vessel mask. Each envelope was subdivided into skeleton segments using perpendicular lines to the vessel, creating neural envelope skeleton segments roughly corresponding to each vessel skeleton segment. Neuronal $\Delta F(t)/\langle F\rangle$ values were averaged within each neural envelope skeleton segment and stored for further analysis. From here, neuronal phase gradients were calculated in the same way as vessel phase gradients, with locations equal to the average pixel location in each segment.

Stimulation paradigms

To study the driven vascular response, various stimuli were applied at frequencies near the vasomotor frequency. In AO-2P stimulation experiments (Figures 5A, 5B, and S3), air puffs were directed to all vibrissae contralateral to the imaging window. Stimulation consisted of three 10 ms puffs separated by 150 ms delays, repeated every 10 s for a stimulation rate of 0.1 Hz. In widefield imaging experiments, stimulation was directed to the right, left, or both vibrissae and the stimulation frequency was varied around 0.1 Hz (Figure 5C).

In some widefield imaging experiments visual stimulation was also presented. Visual stimulation consisted of a 2 s, 455 nm light pulse at 50 Hz and 50% duty cycle directed via optical fiber at the right or left eye (ThorLabs no. M455L3). This pulse was repeated at various frequencies near 0.1 Hz. Some widefield experiments also contained audio stimulation, but only the resting state portion of these experiments were used. Stimulation parameters used for each widefield imaging experiment are listed in Table S1.

QUANTIFICATION AND STATISTICAL ANALYSIS

Spectral methods
All estimates of spectra, coherence, and phase were calculated using multitaper spectral methods.[103,107] The number of tapers was *2TW – 1* where *T* is the acquisition length and *W* is the half-bandwidth.

Resting state spectral estimation from widefield data
Widefield data were acquired in 500 s windows and was processed using a 0.02 Hz half-bandwidth for averaging over 19 Slepian tapers unless otherwise specified. The spectra from each pixel were averaged to form each trial's resting state spectrum. This spectrum was used to estimate the peak vasomotor frequency using MATLAB's "findpeaks" function in a user-defined frequency band of approximately 0.02–0.4 Hz. The frequency that maximized spectral power within this range was defined as the peak vasomotor frequency and was used for subsequent analyses. The space-frequency singular value decomposition (SVD) was calculated over the same number of tapers, as described.[52,108] We show the dominant mode's magnitude and phase at the peak vasomotor frequency (Figure 4A; Table S1).

Spectral estimation for PAs during periodic stimulation
For the PA stimulated dataset we detected and separated out stimulus-induced periodic activity from all other activity in the frequency domain.[109,110] An F-test was used to identify frequencies for which spectral power differed significantly from the local smooth spectrum. These detected line components were separated, and the reported power spectrum consists of significant line component amplitudes plus the residual power (Figure 5A).

Propagation analysis
We used the linear dispersion relation $c = \frac{2\pi}{|k_{vaso}|} f_{vaso}$ to estimate propagation speed from each joint distribution of frequency versus phase gradient. Measurements were binned by 10% of the cumulative frequency distribution, and within each bin the R^2-weighted median f_{vaso} and $|k_{vaso}|$ were calculated (red points in Figures 4C and 5C, and black points in Figure 2F). We fit a line through the origin to these points, whose slope is $c/2\pi$. To calculate the R^2-weighted median f_{vaso} and $|k_{vaso}|$, values within each 10% bin were assigned a normalized weight $w_i = \frac{R_i^2}{\sum_{i=1}^{N} R_i^2}$ where N is the number of vessels in the bin. The f_{vaso} and $|k_{vaso}|$ were arranged in increasing order, and the weighted median was the Mth value, for which $\sum_{i=1}^{M-1} w_i \leq 0.5$ and $\sum_{i=M+1}^{N} w_i \leq 0.5$.

To calculate wave speed uncertainties, bootstrap speed estimates were found by resampling all ($|k_{vaso}|,f_{vaso}$) pairs with replacement, calculating the resulting 10% binned points, R^2-weighted median f_{vaso} and $|k_{vaso}|$, and their slope through the origin. Reported standard errors are the sample standard deviation of the bootstrap speed estimates. Note that for the PA calculation (Figure 2F) inverse-variance weights were used in place of R^2.

Weighted averages and significance tests
Wherever possible, we weighted phase gradients by the R^2 of their source regression to place interest on the goodness of fit of the linear phase progression. This was not possible for PAs, as only two locations were measured. We also weighted diameter and flux modulation values ($2\Delta d/\langle d \rangle$ and $2\Delta q/\langle q \rangle$) by their associated least-squares cosine regression R^2. Slopes β and intercepts $\Delta P/\langle P \rangle$ were weighted by their associated inverse-squared regression coefficient standard error. Here the primary interest was not the goodness of fit of the model (Equation 3), but rather the uncertainty in each measured quantity due to intra-trial variability.

To quantify the observed variability around the weighted means, the variances of all measured quantities (Table 1) were calculated using

$$\sigma_x^2 = \frac{n}{n-1} \left(\langle x^2 \rangle_{wtd} - \langle x \rangle_{wtd}^2 \right).$$

Here x is the quantity of interest, $\langle x \rangle_{wtd}$ denotes the weighted average of x, and n is the number of measurements. Standard deviation values reported in Table 1 are the square root of this weighted variance and reflect the width of the distribution of measurements. To test for differences between slopes (β) we used two-sample t-tests, which are well approximated by Z-tests, with optimal estimates $\overline{B}_g^*$ being the weighted mean β within each group g and optimal estimate standard error being $\overline{s}_g = \sqrt{\frac{1}{\sum_{j=1}^{n} \sigma_{g,j}^{-2}}}$. Here $\sigma_{g,j}$ is the regression coefficient standard error from group g and trial j. The t-test was performed using the test statistic $Z = \frac{\overline{B}_1^* - \overline{B}_2^*}{\sqrt{\overline{s}_1^2 + \overline{s}_2^2}}$ to test H_0: $\beta_1 - \beta_2 = 0$. The same procedure was used in one-sample t-tests for slopes differing from zero with null hypothesis H_0: $\Delta P/\langle P \rangle = 0$.

Vessel length and estimated speed
We consider systematic errors as opposed to the above random error in measured quantities. A previous quantification of the propagation speeds in pial arterioles reports a median speed of 0.41 mm/s (Table 1) across small, i.e., 510 by 510 μm and 255 by 255 μm

fields of view in a mouse with an open craniotomy.[27] These authors also introduced the use of a Ca^{2+}-indicator in smooth muscle cells, for which they report the higher median speed of 0.97 mm/s (Table 1).[27] Contradictions aside, how can we reconcile these data with the current findings? First, disagreements between diameter measurements inferred from a Ca^{2+}-indicator and those from scanning the cross-section of a vessel may result from movement of the brain, which is avoided by placing "a curtain of light" orthogonal through the vessel (Figure 1A). Next, we observe that Ca^{2+} phase progression is a highly variable function of distance on the submillimeter scale (Figure S8A). Short segments of this typical phase progression biased the observations toward larger values of k_{vaso} and therefore smaller speeds (blue example fits in Figure S8A). To test if this could account for the discrepancies in measured speed, we analyzed our pial dataset (Figure 4A) at various vessel segment lengths (Figure S8B). The estimates of wave-speed only asymptote to a constant when the vessel lengths exceed 1.2 mm (black line represents the dataset used in this paper, Figure S8B). Thus, we conclude that past results[27] were apparently confounded by short vessel lengths.

Resistance model

We consider a one-loop network with two resistors (inset in Figure 1J) to interpret the value of β in Equation 3. One resistor represents the pial arterioles, with value $r_{arterioles}$, and the other represents the parenchymal network, predominantly capillaries, with value $r_{capillaries}$; we subsume a small penetrating vessel resistance in $r_{capillaries}$ and recall that the three-dimensional network of capillaries supports a single resistor approximation.[21] Kirchhoff's law gives $qr_{arterioles} + qr_{capillaries} - V = 0$, where V is the pressure drop across the network. Taking the diameter dependence of resistance as $r_{arterioles} \propto d^{-4}$, calculating $\delta q/\delta d$, and using the definition of β (Equation 3) with $\Delta P/P = 0$ gives an expression for the fraction of resistance in the capillaries as (Equation 4)

$$\frac{r_{capillaries}}{r_{capillaries} + r_{arterioles}} = 1 - \frac{\beta}{4}.$$

Modal areal analysis

Widefield data from 9 animals were grouped and analyzed separately (Figures 6 and S7). It was therefore necessary to obtain $\Delta F(t)/\langle F \rangle$ on a common set of spatial points within each animal, given small differences in vessel morphology between trials. To accomplish this, vascular and neuronal data were interpolated by solving Laplace's equation, $\nabla^2[\Delta F(t)/\langle F \rangle] = 0$, at every non-mask pixel to populate originally masked-out regions. For each vascular data frame, $\Delta F(t)/\langle F \rangle$ in the vessel mask was kept fixed and served as a type 1 (fixed-value) boundary. A type 2 boundary was imposed at the midline ($\partial[\Delta F(t)/\langle F \rangle]/\partial n = 0$ for n normal to the midline) and $\Delta F(t)/\langle F \rangle$ far (approximately 5 mm) from the window edge was set to 0. Laplace's equation was discretized using central differences, written for each pixel that didn't belong to the vessel mask, and solved using MATLAB's "mldivide". The solutions were identical to the raw data in the vessel mask and were smoothly varying interpolations with no local maxima or minima in non-mask regions. The same procedure was used to interpolate the neural $\Delta F(t)/\langle F \rangle$ data for pixels in the vessel mask, using only type 1 boundaries far from the window edge and at neural mask pixels.

Graph-Filtered Temporal Dictionary (GraFT) procedure

GraFT is a matrix factorization method with an emphasis on extracting temporal dynamics and corresponding (potentially) non-contiguous spatial profiles. In brief, with GraFT we model the observed data as $Y_{total} = DS + E$, where D is the time-trace dictionary, of size $N_{trial}T$ by N_{mode}, and the spatial mode matrix S (of size N_{mode} by N_{pixel}) represents the corresponding shared spatial presence coefficients across all trials. Each of the rows of S, normalized between 0 and 1, can be reshaped as an image of the size of the recorded FOV to obtain a weighted spatial map (Figure 6A). Each such map corresponds to a temporal mode in D and indicates the pixels that the temporal mode is active in. The corresponding column of the temporal mode in D is a concatenation of the time-traces of all trials of that spatial mode. The matrix E, of size $N_{trial}T$ by N_{pixel}, is i.i.d. Gaussian noise. To obtain estimates of D and S, GraFT solves the optimization problem

$$argmin_{D,S} ||Y_{total} - DS||_F^2 + R_S(S) + R_D(D)$$

by iteratively updating D with a dictionary learning step and updating S with a graph-regularized sparse coding step. The terms $R_S(S)$ and $R_D(D)$ are specific regularizations terms for the spatial and temporal components, respectively, and we refer the reader to[56] for more details of the algorithm.

We apply the above procedure in similar fashion to the vascular data to obtain the vascular spatial modes and time traces. For each recorded trial in our data, we let Y_{trial} be the interpolated data matrix of the observed neuronal/vascular fluorescent activity $\Delta F(t)/\langle F \rangle$. The size of Y_{trial} is $T \times N_{pixel}$, where T is the fixed total number of time frames in each trial and N_{pixel} is the number of pixels in the field-of-view. Given repeated trials of resting-state dynamics of the same animal, we assume that there is a set of patterns of spatial activation, i.e., groups of pixels with similar temporal activity, that are shared across trials. We therefore align all the trials to the same set of spatial coordinates using MATLAB's *imregdemons* function applied to the neural masks. We then concatenated all data matrices across trials along the time dimension, yielding a single data matrix, Y_{total}, of dimension $N_{trial}T$ by N_{pixel} for each animal,

where N_{trial} is the total number of trials. Lastly, we applied GRAFT learning[56] to the data matrix Y_{total} of each animal to obtain its shared spatial modes and temporal traces across trials. The parameter N_{mode} is the total number of modes we chose to decompose our data into; we set $N_{\text{mode}} = 10$ for the data in Figures 6 and S7.

Spatial correlation

To match the neuronal spatial modes with the vascular spatial modes, we computed their pairwise two-dimensional correlation coefficient R, using the MATLAB "corr2" function, and reported the pairwise correlation matrix. The matrix is sorted so that the diagonal has decreasing values. This also gives an order of matching between the neuronal and vascular modes.

Spectral coherence

To examine the spectral relationship between the temporal modes, we computed the pairwise spectral coherence between all dictionary traces using the function "coherency" in Chronux. We reported the matrix of pairwise coherence using node ordering obtained from spatial mode matching.

Linear prediction analysis

To predict vascular response from neuronal activity, we first applied the above modal analysis[56] to the neuronal activity matrix, obtaining per-trial neuronal temporal modes. This can be viewed as a dimensionality reduction step on the neuronal data,[111] where the N_{mode} temporal modes were subsequently used for prediction of pixel-wise vascular response. We adopted a linear regression model with lag for the prediction analysis. Formally, let $y_i^k(t)$ denotes the vascular response time trace of the i-th pixel of trial k (i-th column of Y_k), and let $d_j^k(t)$ denotes the j-th temporal mode of trial k (the j-th column of D_k). We then model the pixel vascular time series as a weighted sum over the temporal modes with possible lags

$$y_i^k(t) = \sum_{j=1}^{N_{\text{mode}}} a_{ij}^k d_j^k(t - \tau^k) + \epsilon,$$

where τ^k is the trial dependent time lag variable and ϵ is assumed to be i.i.d. Gaussian noise and a_{ij}^k are the regression coefficients, i.e., weighting each of the temporal modes to reconstruct the pixel-wise time trace y_i^k. For a fixed τ value, we can obtain an analytical least squares solution of the model, and we fit the model over a range of τ values, i.e., –14 s–14 s, interleaved by 0.2 s, over all pixels and trials in the training set. A leave-one-out approach was used to fit and test the model performance, such that in each instance one single trial is used as a hold-out testing trial, and all the rest N_{trial} - 1 trials are used as training trials to fit the regression model. After fitting over the training trials, we found the best lag τ^k for each training trial by selecting the τ_{opt}^k value that yielded the highest pixel-averaged R^2 for that trial. The median over all such τ_{opt}^k on the N_{trial} - 1 training trials was then used as the estimate for lag on the testing trial. To obtain the pixel-wise linear coefficient estimate on the testing trial, we average the regression coefficients a_{ij}^k corresponding to τ_{opt}^k on each training trial k over all trials. Using the estimated a_{ij} and τ on the testing trial, we predict the testing trial vascular response from its neuronal temporal modes and evaluate the R^2 score with respect to the ground truth vascular response of the trial. We repeat this regression analysis for predicting pixel-wise neuronal time-traces from vascular temporal modes.

Code

All data were analyzed and plotted with custom-written MATLAB code. The MATLAB implementation of the GraFT algorithm can be found in https://github.com/adamshch/GraFT-analysis. The MATLAB package Chronux found at https://www.chronux.org is used for spectral analysis. All other code used can be found at https://neurophysics.ucsd.edu/software.php.